Crucial Role of Lateral Size for Graphene Oxide in Activating Macrophages and Stimulating Pro-inflammatory Responses in Cells and Animals

Juan Ma,[†] Rui Liu,[†] Xiang Wang,[‡] Qian Liu,[†] Yunan Chen,[†] Russell P. Valle,[§] Yi Y. Zuo,[§] Tian Xia,[*,‡] and Sijin Liu[*,†]

[†]State Key Laboratory of Environmental Chemistry and Ecotoxicology, Research Center for Eco-Environmental Sciences, Chinese Academy of Sciences, Beijing 100085, China, [‡]Division of NanoMedicine, Department of Medicine, University of California, Los Angeles, California 90095, United States, and [§]Department of Mechanical Engineering, University of Hawaii at Manoa, Honolulu, Hawaii 96822, United States

ABSTRACT Graphene oxide (GO) is increasingly used in biomedical applications because it possesses not only the unique properties of graphene including large surface area and flexibility but also hydrophilicity and dispersibility in aqueous solutions. However, there are conflicting results on its biocompatibility and biosafety partially due to large variations in physicochemical properties of GO, and the role of these properties including lateral size in the biological or toxicological effects of GO is still unclear. In this study, we focused on the role of lateral size by preparing a panel of GO samples with differential lateral sizes using the same starting material. We found that, in comparison to its smaller counterpart, larger GO showed a stronger adsorption onto the plasma membrane with less phagocytosis, which elicited more robust interaction with toll-like receptors and more potent activation of NF-κB pathways. By contrast, smaller GO sheets were more likely taken up by cells. As a result, larger GO promoted greater M1 polarization, associated with enhanced production of inflammatory cytokines and recruitment of immune cells. The *in vitro* results correlated well with local and systemic inflammatory responses after GO administration into the abdominal cavity, lung, or bloodstream through the tail vein. Together, our study delineated the size-dependent M1 induction of macrophages and pro-inflammatory responses of GO *in vitro* and *in vivo*. Our data also unearthed the detailed mechanism underlying these effects: a size-dependent interaction between GO and the plasma membrane.

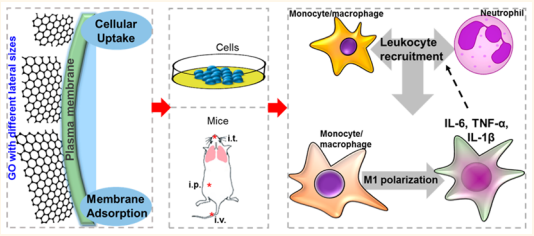

KEYWORDS: graphene oxide · macrophages · plasma membrane · pro-inflammatory responses · nanotoxicology

Graphene derivatives (such as graphene oxide, GO) possess unique physicochemical properties including large surface area, flexibility, and good dispersibility in various solutions.[1,2] Thus, GOs are increasingly used in biomedical applications including sensors, optical imaging, antibiotics, and drug/gene delivery.[3,4] The expanding use of GO in biomedicine will certainly increase the opportunity of human exposure, and this has raised general concerns on its safety. To achieve the maximal potential in biomedical uses of GO, it is necessary to determine its hazard potential and understand the mechanisms of action.

To date, there are conflicting results on the biocompatibility of GO. Some reports suggest that GO is biologically safe, while others draw different conclusions.[4−8] For those who demonstrated GO toxicity, there is an uncertainty on the exact physicochemical properties (*e.g.*, lateral size, thickness, geometry, and functional groups) that are responsible for its adverse effects.[9] Although researchers have recognized that the lateral size of GO may play an important role in determining its biological effects,[10,11] the key question remains unanswered: how the lateral size dictates cellular responses to GO. First, the interface between GO and the plasma membrane has not been investigated in depth thus far. Second, there is no clear insight about how sensing molecules on the membrane surface respond to GO, as well as the role of the GO lateral size in determining membrane adsorption and intracellular uptake of GO. Third, studies

* Address correspondence to (S. Liu) sjliu@rcees.ac.cn; (T. Xia) txia@ucla.edu.

Received for review July 30, 2015 and accepted September 21, 2015.

Published online September 21, 2015
10.1021/acsnano.5b04751

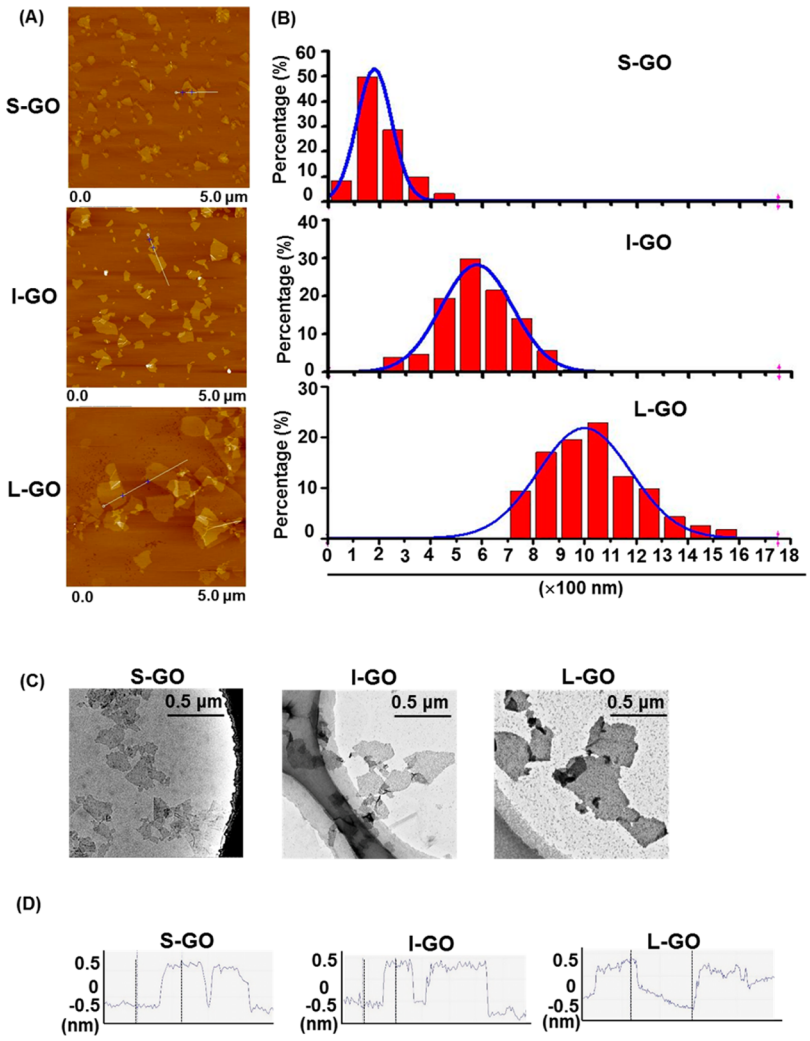

Figure 1. Morphological characterization of GO samples. (A) Representative AFM topography of S-GO, I-GO, and L-GO. (B) Histogram of GO size distribution. The histograms were developed by counting 280−300 sheets for each sample, with Gaussian fit curves shown in each histogram. (C) TEM images of S-GO, I-GO, and L-GO. (D) Analysis of the height of S-GO, I-GO, and L-GO through AFM.

were often carried out either *in vitro* or *in vivo* without showing their correlations. In addition, the signaling pathways responsible for size-related GO toxicity remain poorly understood.

Herein, we set out to determine the hazard potential of GO and the impact of lateral size on GO-induced biological or toxicological effects. Using the same starting material, we prepared a battery of GO samples with different lateral sizes without changing other properties. We investigated their effects on monocytes/macrophages that are the first line of defense at the portal-of-entry against foreign agents and release substances to activate other immune cells. We performed studies on GO-induced local and systemic pro-inflammatory effects after administration into the abdominal cavity, lung, or bloodstream through the tail vein. We demonstrated the distinct effects of GO with different lateral sizes in inducing macrophage M1 polarization and pro-inflammatory effects *in vitro* and *in vivo*. We also determined the molecular mechanism of GO-induced inflammation that involved the toll-like receptors (TLRs) and NF-κB pathways.

RESULTS

Preparation of GO with Distinct Lateral Sizes. To clarify the role of lateral size in the interaction between GO and cells, we prepared a series of GO samples with different lateral sizes through breakdown of the same starting material. Since the size range for GO in biomedical applications is usually from ~50 to ~1000 nm,[12−15] our GO samples were prepared in a comparable lateral size range. As shown in Figure 1A, the morphology of GO samples was visualized by atomic force microscopy (AFM). The size distribution analysis showed most (>95%) GO sheets ranged from 50 to 350 nm for S-GO (smallest), from 350 to 750 nm for I-GO (intermediate), and from 750 to 1300 nm for L-GO (largest), respectively (Figure 1B, $P < 0.001$). The difference in lateral size for GO samples was confirmed by transmission electron microscopy (TEM) (Figure 1C).

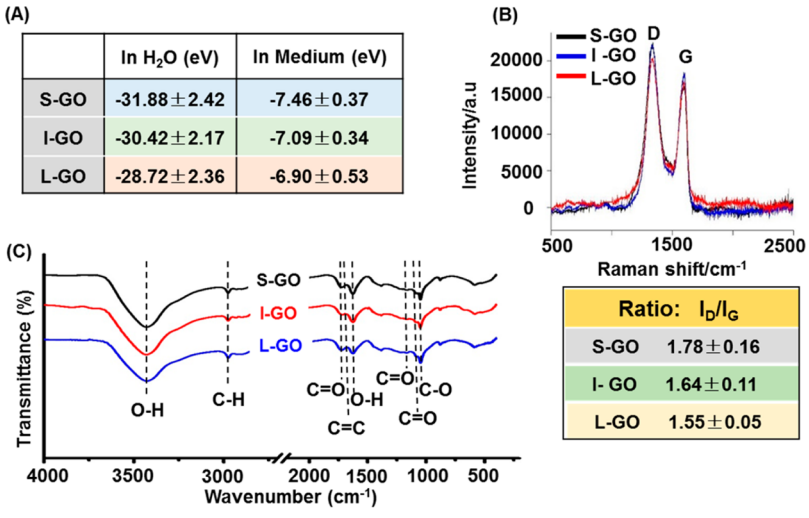

(A)

	In H_2O (eV)	In Medium (eV)
S-GO	-31.88±2.42	-7.46±0.37
I-GO	-30.42±2.17	-7.09±0.34
L-GO	-28.72±2.36	-6.90±0.53

Ratio: I_D/I_G	
S-GO	1.78±0.16
I- GO	1.64±0.11
L-GO	1.55±0.05

(E)

Composition	C-C/C=C	C=O	O=C-OH	C-OH
S-GO	0.43±0.01	0.50±0.01	0.05±0.01	0.02±0.00
I-GO	0.42±0.01	0.50±0.00	0.05±0.01	0.02±0.00
L-GO	0.43±0.01	0.51±0.01	0.05±0.02	0.00±0.01

Figure 2. Physicochemical characterization of GO samples. (A) Zeta potential of S-GO, I-GO, and L-GO in water and in cell culture medium (n = 3). (B) Raman spectrum and curve fitting of D band and G band. The average ratio of ID/IG is shown in the lower panel (n = 9). (C) Identification of functional groups on the GO surface by FTIR spectrum (range: 4000−400 cm^{-1}). (D) Characterization of surface composition of GO samples by XPS. (E) Quantified data for the portions of functional groups (range: 0−1.0, n = 3).

In addition, AFM showed that the average thickness was approximately 1.0 nm for all these samples (Figure 1D), indicating that they were composed of single-layered graphene sheets.[16] These data suggested that we have successfully prepared single-layered GO samples with different average lateral sizes.

To make sure that the sample preparation processes did not change physicochemical properties other than the lateral size, we performed detailed physiochemical characterizations for these GO samples. Surface charge was analyzed by zeta-potential assessment. As shown in Figure 2A, suspended either in Milli-Q water or in cell culture medium, these GO samples were similarly negatively charged. The UV−vis spectrum showed an absorption peak at 227 nm for all these GO samples (Supplementary Figure 1), which was similar to the reported feature range of 227−231 nm for GO.[17−19] The λ_{max} determined by $\pi \rightarrow \pi^*$ transitions was constant among these GO samples, and the shoulder peak attributed to n $\rightarrow \pi^*$ transitions of the carbonyl groups was also found at around ∼300 nm in the UV−vis profile for all GO samples (Supplementary Figure 1), which was consistent with a GO sheet with a size in the range of ∼300 to ∼2000 nm.[18,20,21] Furthermore, Raman spectra showed similar basal structure profiles with a characteristic D peak (1331 cm^{-1}) and G peak (1596 cm^{-1}) (Figure 2B) for all the GO samples, consistent with published data.[22] The D band represents the presence of disorder in sp^2 hexagonal carbon, whereas the G band indicates stretching of C−C bonds in graphitic materials.[23,24] The ratio of ID (intensity of D band)/IG (intensity of G band) is oftentimes applied to reflect the quantity of structural defects in graphitic materials.[25−27] After calculation, a similar ID/IG ratio was found for all three as-prepared GO samples: 1.78, 1.64, and 1.55 for S-GO, I-GO, and L-GO, respectively, without statistically significant differences (Figure 2B, lower panel, $P > 0.05$), indicating comparable structural defects in these GO samples.

Fourier transform infrared (FTIR) spectroscopy was performed to explore the surface groups of the GO samples, and the results are illustrated in Figure 2C. The peaks at 3420 and 1620 cm^{-1} represented the absorbance of O−H stretching vibrations, whereas bands denoting C−O and C═O stretching of the COOH group were located at 1042 and 1073 cm^{-1}. Meanwhile, the C═O vibration band was identified at 1170 cm^{-1}, and the band corresponding to C═O stretching vibration of COOH was located at 1740 cm^{-1}. Furthermore, bands representative of C−H stretching were recognized at 3000−2800 cm^{-1}. Moreover, X-ray photoelectron spectroscopy (XPS) displayed similar profiles for all GO samples, with characteristic peaks at 284.4, 286, 286.5, and 288.3 eV, representing C−C/C═C, C−OH, C═O, and O═C−OH groups, respectively (Figure 2D). The quantitative analysis of each group showed that the C−OH content was slightly increased in S-GO and I-GO, relative to L-GO; however, the total amount of C═O and O═C−OH remained consistent for all GO samples (Figure 2E). Additionally, the C−C/C═C content was constant for these GO samples (Figure 2E). Taken together, these characterization data demonstrated that S-GO, I-GO, and L-GO samples showed comparable physicochemical properties except lateral size differences.

GO Induced Lateral Size-Dependent Pro-inflammatory Responses in Macrophages. We used J774.A1 macrophages as the cellular model to study the GO-induced pro-inflammatory effect. First, we performed the cytotoxicity screening with the live/dead assay, which showed progressive decrease in cell viability by L-GO treatment starting at 20 μg/mL at 24 h (Supplementary Figure 2A, $P < 0.05$). Although I-GO and S-GO could also reduce the cell viability of J774.A1 cells at 20 μg/mL, they are significantly less toxic than L-GO at 12 and 24 h (Supplementary Figure 2B, $P < 0.05$). This finding was further confirmed by PI staining (Supplementary Figure 2C, $P < 0.05$). These results demonstrated that GO induced cell death in J774.A1 cells in a size-dependent manner at the same mass dosage, and we chose 20 μg/mL in the following experiments because a large percentage of cells remained viable after 24 h treatment.

Previous reports showed that GO treatment could trigger inflammatory responses including the production of inflammatory cytokines by macrophages.[8,28,29] Thus, we determined the cytokine production in J774A.1 cells in response to GO treatment. We found that GO induced exaggerated mRNA expression of pro-inflammatory TNF-α and IL-6 in J774.A1 cells at 20 μg/mL for 24 h, and the mRNA expression levels by GOs correlated well with the lateral size of GO, which ranked as S-GO < I-GO < L-GO (Supplementary Figure 3A,B, $P < 0.05$). ELISA assay validated the size-dependent induction of TNF-α and IL-6 in J774.A1 cells (Figure 3A,B, $P < 0.05$). A similar observation on mRNA expression levels of TNF-α and IL-1β was made in human macrophage THP-1 cells by S-GO, I-GO, and L-GO at 20 μg/mL for 24 h (Supplementary Figure 4A,B, $P < 0.05$). These data showed that GO could induce pro-inflammatory effects in a size-dependent manner, and the most significant difference was found between L-GO and S-GO. Therefore, we compared the effects of L-GO and S-GO for the following investigations.

L-GO Induced Significantly Higher Inflammatory Responses than S-GO in Animals after Intraperitoneal Injection (*ip*) administration. To test whether the *in vitro* findings also hold true *in vivo*, we tested the effects of GO in mice delivered by *ip* injection because the abdominal cavity is an ideal site to study macrophage activation and it has also been used as a surrogate for the mesothelial lining of the chest cavity.[30,31] The dose used in the current study was comparatively lower than other studies on the *in vivo* biodistribution and toxicity of GO,[32−34] and the GO dosage we used here did not cause overt toxicities to animals, as manifested by the absence of weight loss and abnormal activities (including eating and drinking). After *ip* administration, we studied local inflammation using lavage from the peritoneal cavity and systemic inflammation using serum. For local inflammation, the peritoneal cavity for each mouse was thoroughly lavaged with cold phosphate-buffered saline (PBS) post-GO-exposure, similar to a previous report.[35] As shown in Figure 3C, the total protein levels increased significantly to 3-fold or 4-fold than control for S-GO- or L-GO-treated mice, respectively ($P < 0.05$). The concentration of TNF-α in the lavage was significantly increased (Figure 3D, $P < 0.001$), with the TNF-α level in L-GO-treated mice being 6 times more than that in the S-GO-treated mice (Figure 3D, $P < 0.001$). A similar pattern was found for IL-6 secretion between the two treatments, although the difference is smaller (Figure 3E, $P < 0.05$). In addition to the induction of local inflammation in the abdominal cavity, considerable systemic inflammation was also observed. We found a significant increase in IL-6 and TNF-α production in serum from GO-treated mice, and L-GO induced significantly higher cytokine production than S-GO (Figure 3F,G, $P < 0.05$), which was consistent with the findings from *in vitro* assays and analysis with peritoneal lavage. Bacterial lipopolysaccharides (LPS), a positive control, induced systemic inflammation in mice (Supplementary Figure 5A,B). These data suggested that GO could induce enhanced inflammatory cytokine production locally in the abdominal cavity and systemically in blood for mice after GO exposure. The magnitude of the pro-inflammatory effect was closely related to the lateral size of GO, and L-GO was significantly more potent than S-GO.

Macrophages also play a critical role in recruiting and activating other immune cells to enhance the pro-inflammatory responses through secreting signaling proteins.[36−38] As shown in Figure 3H, the total number

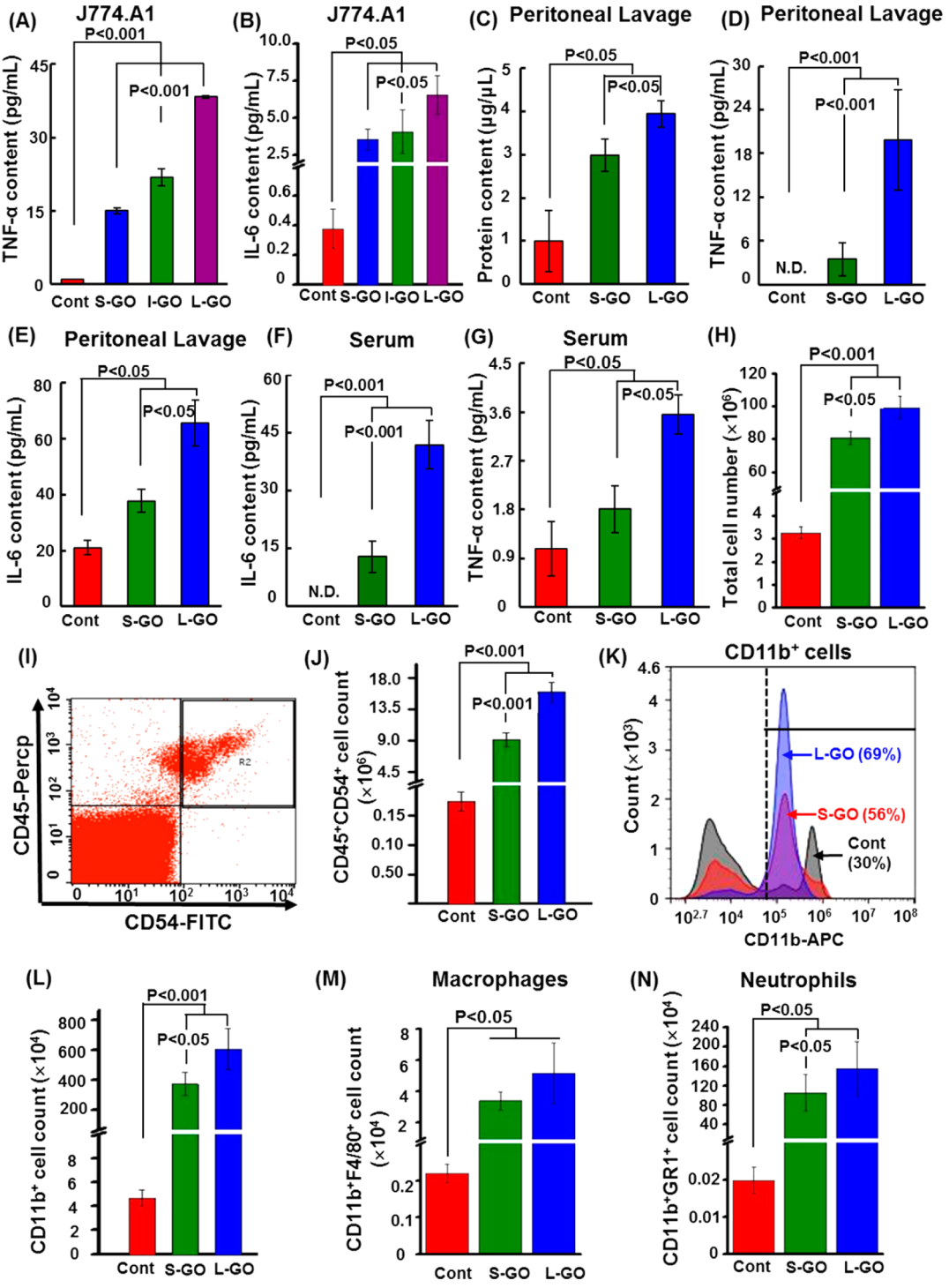

Figure 3. GO induced macrophage activation in a size-dependent manner. (A, B) Protein concentrations of TNF-α and IL-6 secreted in cell culture medium. After GO treatment at 20 μg/mL for 24 h, (A) TNF-α and (B) IL-6 in culture medium were assayed through ELISA (n = 6). (C–N) After GO administration in mice, the peritoneal lavages and peripheral blood were collected; (C) content of total exudation proteins collected from the peritoneal cavities; concentrations of (D) TNF-α and (E) IL-6 in the total exudation proteins; levels of (F) IL-6 and (G) TNF-α in sera; (H) number of collected cells in peritoneal lavages with exclusion of RBCs; (I) selection of $CD45^+CD54^+$ cells for further analysis; (J) number of $CD45^+CD54^+$ cells in peritoneal lavages; (K) percentages of $CD11b^+$ subpopulation of $CD45^+CD54^+$ cells; data were acquired from 20 000 cells per sample; (L) number of $CD11b^+$ subpopulation of $CD45^+CD54^+$ cells; (M) total number of $CD11b^+$ $F4/80^+$ subpopulation of $CD45^+CD54^+$ cells; (N) total number of $CD11b^+Gr1^+$ subpopulation among $CD45^+CD54^+$ cells. There were 6 mice per group (n = 6). ND: not detectable.

of peritoneal cells was increased by more than 24-fold or 30-fold in the lavage after S-GO or L-GO exposure, respectively, compared to untreated mice ($P < 0.001$), suggesting significant recruitment of cells into the

peritoneal cavities by GO. Furthermore, recruited cell populations were carefully differentiated by flow cytometry analysis (FACS) (Figure 3I). Enhanced recruitment of leukocytes was found in the peritoneal cavities of mice upon GO exposure, as shown by mostly 84-fold and 136-fold increases of the $CD45^+CD54^+$ population (representative of recruited leukocytes[39−43]) upon S-GO and L-GO treatment, respectively, and L-GO is significantly higher than S-GO (Figure 3I,J, $P < 0.001$).

The acute phase of inflammation involves extravasation and migration of inflammatory leukocytes to infected sites.[44] For instance, activated macrophages secrete inflammatory cytokines (such as TNF-α and IL-6), which recruit more monocytes/macrophages and other types of leukocytes (*e.g.*, neutrophils) to the affected area as a hallmark of acute inflammation.[44] CD11b is a canonical surface marker of myeloid cells including monocytes, macrophages, and neutrophils.[45,46] Our FACS analysis showed that the percentage of $CD11b^+$ subpopulation cells among the $CD45^+CD54^+$ population was notably increased in S-GO-treated mice (56%) and L-GO-treated mice (69%), compared to untreated mice (30%) (Figure 3K, $P < 0.05$). The number of $CD11b^+$ subpopulation among the $CD45^+CD54^+$ cells was strikingly increased by more than 90-fold for S-GO and 129-fold for L-GO, compared to untreated mice (Figure 3L, $P < 0.001$). As shown in Figure 3M,N, within the $CD11b^+$ cell population, a large proportion was stained with F4/80-positive ($CD11b^+F4/80^+$ cells, referring to monocytes/macrophages) or Gr1-positive ($CD11b^+Gr1^+$ cells, namely, neutrophils) cells in S-GO- or L-GO-treated mice, compared to that in untreated cells ($P < 0.05$). The total number of $CD11b^+F4/80^+$ subpopulation cells was increased by 15-fold and 24-fold in the peritoneal cavities of mice challenged by S-GO and L-GO, respectively (Figure 3M, $P < 0.05$), whereas the total number of $CD11b^+Gr1^+$ subpopulation cells was elevated by 5321 times and 7811 times in the peritoneal cavities of S-GO-treated mice and L-GO-treated mice, respectively, compared to that in untreated mice (Figure 3N, $P < 0.001$). Considering the difference between S-GO and L-GO, there was an approximately 60% increase in the total number of $CD11b^+F4/80^+$ subpopulation and $CD11b^+Gr1^+$ subpopulation cells in L-GO-treated mice compared to S-GO-administrated mice (Figure 3M,N, $P < 0.05$). These results suggested that GO-activated macrophages recruited inflammatory cells including monocytes/macrophages and neutrophils into peritoneal cavities, and L-GO elicited a greater effect on inflammatory cell recruitment than S-GO, which was consistent with the *in vitro* results (Figure 3A,B and Supplementary Figures 3 and 4).

L-GO Induced Higher Inflammatory Responses in Lung through Oropharyngeal Aspiration (*it*) and in Blood through Intravenous (*iv*) Injection than S-GO. To test pro-inflammatory responses induced by S-GO and L-GO administered *via* other delivery routes, lung exposure by *it* instillation and blood exposure *via* tail vein injection were performed accordingly. After 72 h exposure for both cases, the degree of inflammatory responses was assessed using similar assays to those described above for *ip* GO exposure. As shown in Figure 4A, the level of total protein in bronchoalveolar lavage (BAL) fluid was significantly increased more than 1.8-fold or 2.4-fold in S-GO- or L-GO-treated mice, respectively, compared to untreated mice ($P < 0.05$). IL-6 concentration in BAL fluid was elevated 1.3-fold in S-GO-treated mice and 2.5-fold in L-GO-treated mice, compared to untreated mice (Figure 4B, $P < 0.05$). Recruitment of inflammatory cells into the lung was also determined. As shown in Figure 4C, the total number of cells in BAL fluid was increased by 2.6-fold or 4.1-fold in mice upon S-GO or L-GO administration, respectively, compared to untreated mice ($P < 0.001$), suggesting increased cell recruitment into the lungs by GO. $CD45^+CD54^+$ leukocytes were increasingly recruited in BAL fluid by 6-fold or 12-fold in mice treated by S-GO or L-GO, respectively, relative to that in untreated mice (Figure 4D, $P < 0.05$). Further analysis of the recruited cells showed a great increase of $CD11b^+$ cells in the $CD45^+CD45^+$ population, with a 55-fold or 232-fold increase for S-GO- or L-GO-treated mice, respectively, relative to untreated mice (Figure 4E, $P < 0.05$). Of the $CD11b^+$ subpopulation, marked accumulations of $CD11b^+F4/80^+$ subpopulation cells and $CD11b^+Gr1^+$ subpopulation cells were demonstrated in BAL fluid from mice challenged by S-GO or L-GO (approximately 80-fold for $CD11b^+F4/80^+$ and 19-fold for $CD11b^+Gr1^+$ subpopulations, respectively), especially for L-GO (Figure 4F,G, $P < 0.001$). Moreover, GO induced a 2-fold increase in serum IL-6 in GO-challenged mice (Figure 4H, $P < 0.001$). Notably, L-GO induced significantly higher pulmonary and systemic inflammatory cytokine production and inflammatory cell recruitments than S-GO (Figure 4, $P < 0.05$), consistent with the findings in the peritoneal cavity (Figure 3). In addition to the lung exposure, we also compared the capability of S-GO and L-GO in inducing systemic inflammation by directly administrating GO into the blood through *iv* injection. The IL-6 production in serum increased significantly by GO, and L-GO-induced IL-6 was 2.8-fold higher than S-GO (Supplementary Figure 6A, $P < 0.05$). A similar trend was found for TNF-α secretion between S-GO- and L-GO-treated mice (Supplementary Figure 6B, $P < 0.05$). Collectively, these results further demonstrated lateral size-dependent effects for GO on inducing lung and systemic inflammation.

Lateral Size-Dependent Macrophage Activation into M1 Macrophages That Promoted Inflammation. On the basis of the above *in vitro* and *in vivo* findings, it was reasonable to hypothesize that GO may differentially induce macrophage polarization, which in turn enhanced pro-inflammatory responses, including recruiting

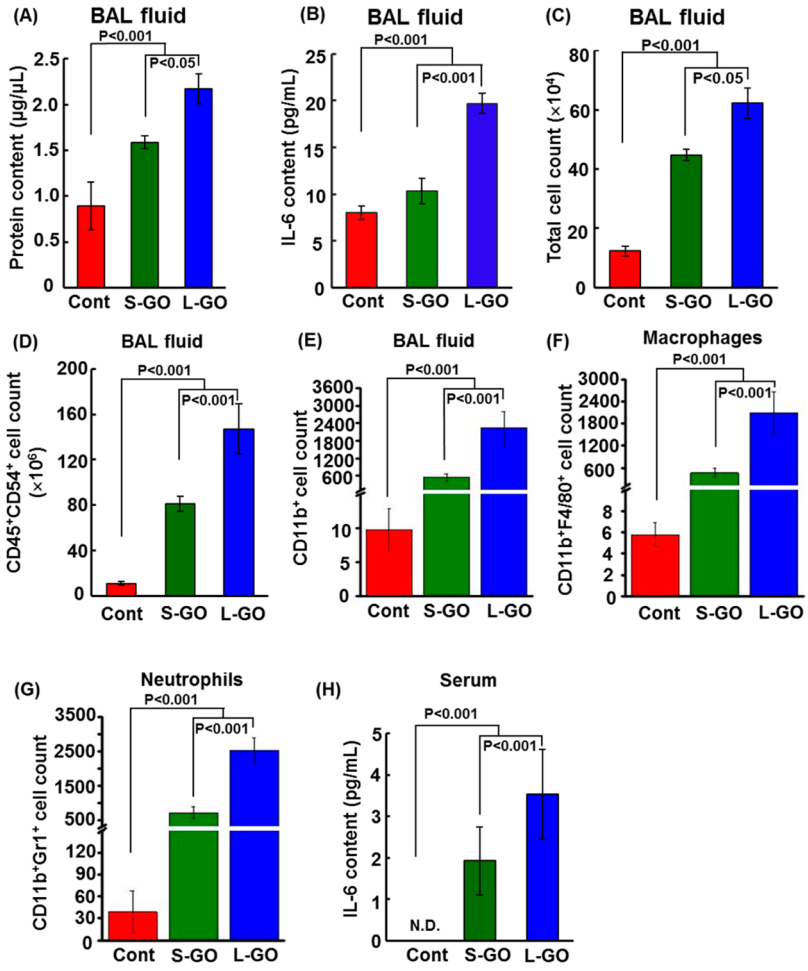

Figure 4. L-GO induced enhanced inflammation in the lung. After GO administration into mouse lungs, the BAL fluid and peripheral blood were collected. (A) Content of total proteins in BAL fluid. (B) Concentrations of IL-6 in BAL fluid. (C) Number of collected cells in BAL fluid with exclusion of RBCs. (D) Number of $CD45^+CD54^+$ cells in BAL with exclusion of RBCs. (E) Number of $CD11b^+$ subpopulation of $CD45^+CD54^+$ cells. (F) Number of $CD11b^+F4/80^+$ subpopulation of $CD45^+CD54^+$ cells. (G) Number of $CD11b^+Gr1^+$ subpopulation among $CD45^+CD54^+$ cells. (H) Levels of IL-6 in sera. There were 6 mice per group (n = 6). ND: not detectable.

leukocytes and stimulating secretion of inflammatory cytokines.[47,48] To validate this hypothesis, we checked the M1/M2 polarization of macrophages through determining the induction of $Arg1^+$ cells (representative of M2 macrophages) or $iNOS^+$ cells (representative of M1 macrophages) by FACS.[20,49−51] After S-GO or L-GO treatment in J774.A1 cells for 24 h, no significant induction of $Arg1^+$ cells was demonstrated compared to untreated cells (Figure 5A, $P > 0.05$). In contrast, induction of $iNOS^+$ cells was significantly increased in GO-treated cells, with a 21-fold increase for S-GO-treated cells and a 31-fold increase for L-GO-treated cells, compared to untreated cells (Figure 5B, $P < 0.001$). Consistent with the FACS results, the iNOS mRNA level was significantly elevated by more than 17-fold upon GO treatment, especially for L-GO (Figure 5C, $P < 0.001$). In support of these data, M1 macrophage-secreted cytokines including TNF-α, IL-6, and IL-1β[52,53] were significantly increased by GO, and L-GO induced significantly higher cytokine production than S-GO (Figures 3 and 4 and Supplementary Figures 3−6, $P < 0.05$). Furthermore, we determined M1 polarization for macrophages in the abdominal cavities of mice after GO administration. In agreement with the *in vitro* results, S-GO significantly increased the induction of $iNOS^+$ cells by 6.6-fold and L-GO induced a 12.2-fold increase compared to untreated cells (Figure 5D, $P < 0.05$). These findings suggested that GO treatment induced macrophage polarization to the M1 phenotype, and L-GO significantly elicited higher M1 macrophage induction than S-GO.

Lateral Size Determined Adsorption and Uptake of GO by Macrophages. To shed light on the molecular mechanisms responsible for size-dependent macrophage activation, we studied the interaction between GO and the plasma membrane and the subsequent uptake of GO by macrophages. As shown in Figure 6A, the Raman mapping spectrum showed characteristic D and G bands in J774.A1 cells treated with 20 μg/mL S-GO or L-GO for 6 h. This result implied a rapid association of GO on the plasma membrane; however, due to the resolution of the confocal micro-Raman spectrometer,

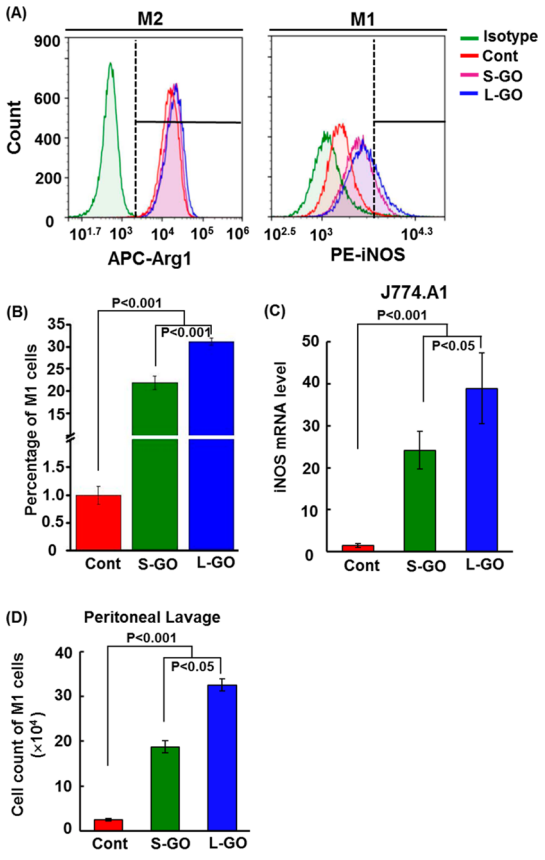

Figure 5. GO induced macrophages to polarize to M1 subtype in a size-dependent manner. (A) Representative histograms showing the numbers of M2 ($Arg1^+$) and M1 ($iNOS^+$) cells. J774.A1 cells were treated with S-GO or L-GO at 20 μg/mL for 24 h, followed by FACS analysis of $Arg1^+$ or $iNOS^+$ cells. Data were acquired from 20 000 cells per sample. (B) Percentages of $iNOS^+$ cells (n = 5). (C) Relative iNOS level in J774.A1 cells upon exposure to S-GO or L-GO at 20 μg/mL for 24 h. HPRT1 was used as control for normalization. (D) Total numbers of $iNOS^+$ cells of selected $CD45^+CD54^+$ subpopulation from the abdominal cavities of mice upon GO administration, as described in Figure 3.

it was difficult to quantify the amount of associated GO and discern the location of the GO: on the membrane or inside the cells.[54,55] To address this issue, we first probed the GO intracellular localization through TEM. As shown in Figure 6B, GO sheets were clearly identified in membrane-bound structures inside cells, most likely in phagosomes within the cytosol, for both S-GO- and L-GO-treated cells. In addition, we can clearly see the flat side of GO sheets attaching in parallel with the plasma membrane in L-GO-treated cells with no sign of being phagocytosed, whereas S-GO sheets could not be readily found on the plasma membrane (Figure 6B). As expected, no sheets could be found in untreated cells (Figure 6B). In addition to TEM, we also used FITC-bovine serum albumin (BSA)-labeled GO to track GO's cellular uptake and localization through laser scanning confocal microscopy. After labeling, a similar amount of FITC-BSA was conjugated on S-GO and L-GO, as reflected by the SDS-PAGE analysis after Coomassie Blue staining (Supplementary Figure 7A). Meanwhile, comparable fluorescence intensity was demonstrated between FITC-BSA-S-GO and FITC-BSA-L-GO (Supplementary Figure 7B). As shown in Figure 7A, while some FITC-BSA-labeled S-GO could be detected on the plasma membrane of J774.A1 cells after 1 h, a large amount of FITC-BSA-labeled L-GO showed adsorption on the plasma membrane (Figure 7A). Also after 1 h incubation, only a small amount of S-GO and L-GO could be observed inside cells (Figure 7A). As the incubation time increased, more GO was taken up into the cells at 3 and 6 h, especially for S-GO-treated cells (Figure 7A). An enlarged image of cellular uptake of S-GO is shown along with the image of an untreated cell in the right panel of Figure 7A. In comparison to S-GO-treated cells, the intracellular fluorescent intensity for L-GO was lower by 30% at 6 h (Figure 7A and Supplementary Figure 8, $P < 0.05$). To quantify the uptake of GO, we use an established FACS technique.[56] The uptake of GO will result in an increase in cellular granularity, as evidenced by the quantitative increase in side scattering (SSC) (Supplementary Figure 9A,B). In support of the above data, the cellular SSC analysis demonstrated that S-GO was engulfed approximately 24−34% more than L-GO over the time course at 3, 6, 12, and 24 h (Figure 7B, $P < 0.05$). These results together demonstrated that L-GO had less cellular uptake, compared to S-GO.

TLRs Were Involved in GO Sensing to Induce Pro-inflammatory Responses. Macrophages sense invading pathogens and particles through a variety of receptors on their membrane,[57] and different receptors are able to discriminate specific components of pathogens.[58] For instance, TLRs, a family of pattern recognition receptors, recognize distinct pathogen-associated molecular patterns,[59,60] as illustrated in Figure 8A. TLR2 detects bacterial peptidoglycans,[61] whereas TLR4 recognizes LPS along with LPS receptors CD14 and MD-2 (encoded by the LY96 gene).[62,63] Activation of TLRs triggers pro-inflammatory responses through an adaptor molecule myeloid differentiation primary-response gene 88 (MyD88).[58] Our above data demonstrated significant pro-inflammatory responses in macrophages in response to GO; thus it would be plausible to interrogate the TLRs that might be activated by GO. An array of TLR inhibitors was employed (Figure 8A,B). Differential effects on TNF-α expression were recorded in J774.A1 cells treated with L-GO in the presence of the inhibitors (Figure 8B). TNF-α expression was significantly repressed by 61% or 34% when TLR2/TLR4 or TLR4 was inhibited by OXPAPC or CLI095, respectively, compared to GO-treated cells without inhibitor pretreatment (Figure 8B, $P < 0.05$). In contrast, inhibition of the organelle membrane molecule TLR9 by ODN2088 did not result in suppression of the TNF-α level (Figure 8B). In addition, the MyD88 inhibitor ST2825[64] significantly inhibited TNF-α mRNA expression by 70% (Figure 8B, $P < 0.05$), supporting the crucial role of

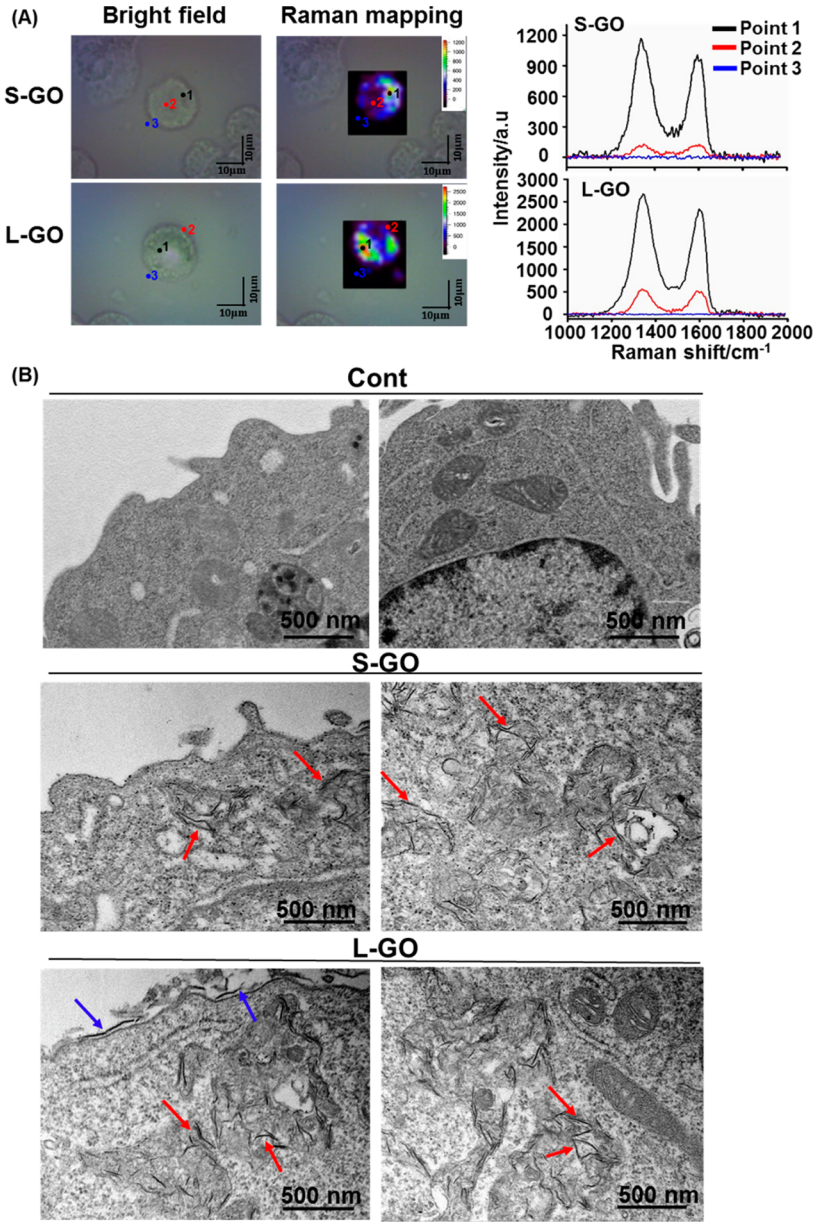

Figure 6. Cellular tracking of GO in J774A.1 cells. (A) Raman mapping spectrum of J774.A1 cells after exposure to 20 μg/mL S-GO and L-GO for 6 h. The red area represents a typical GO signal. A specific Raman spectrum was acquired from 3 target points. Point 1 (in black) represents the site with the highest intensity of Raman signal. Point 2 (in red) was randomly chosen within the cytosolic area, whereas point 3 (in blue) was selected outside the cell. (B) TEM images of J774.A1 cells after exposure to 20 μg/mL S-GO or L-GO for 6 h. Red arrows indicate GO sheets within the cytosol. Blue arrows denote GO sheets on the plasma membrane. TEM images for untreated cells are also shown.

MyD88 at the converging site in transducing upstream stimulatory signals to the downstream pathways.[57,65]

On the basis of the inhibitor data, we chose TLR4 for a detailed study. First, to rule out potential alterations to the concentration of TLR4 on the cell membrane by GO, we investigated the TLR4 levels in the cell membrane portion through Western blotting. As shown in Figure 8C, the protein level of TLR4 was not significantly changed in J774.A1 cells upon treatment with L-GO or S-GO for 12 or 24 h, compared to untreated cells. However, the TLR4 inhibitor CLI095 markedly repressed the expression of TNF-α by approximately 60% in cells after S-GO or L-GO treatment (Figure 8D, $P < 0.05$), suggesting that TLR4 was involved in GO-induced inflammation. To substantiate the regulation of TNF-α expression by GO through TLR4 signaling, we examined TNF-α expression in HEK293/TLR4 cells with TLR4 knock-in in response to GO.[8,66] LPS was used as a positive control to trigger the TLR4 signaling,[67] which increased TNF-α expression up to 40-fold in HEK293/TLR4 cells (Figure 9A, $P < 0.001$), demonstrating that these cells were ideal for studying TLR4 activation. Using these cells, we found L-GO could activate TLR4 signaling and increase TNF-α expression by approximately 2.5-fold, compared to untreated HEK293/TLR4 cells (Figure 9B, $P < 0.05$). In contrast,

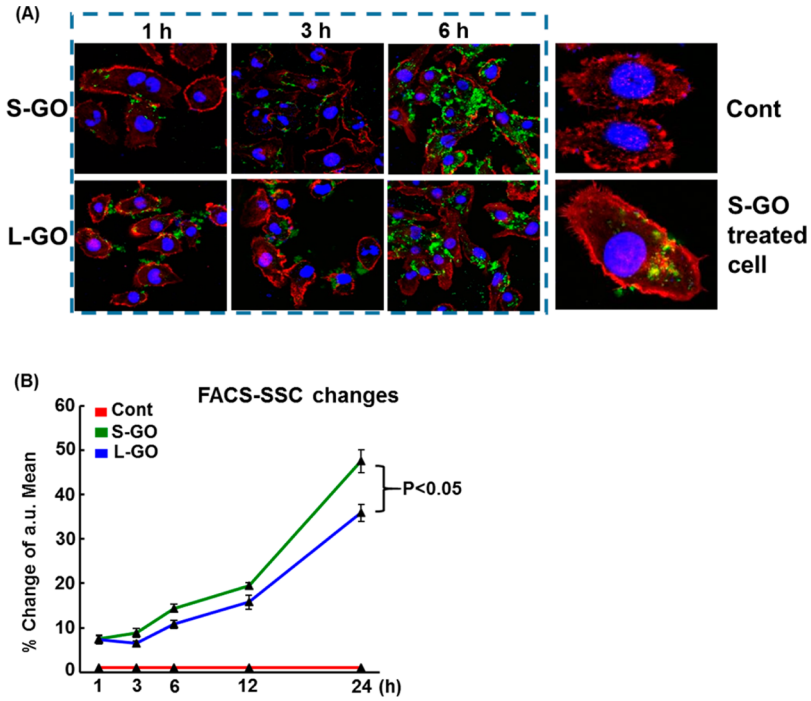

Figure 7. Size-dependent adsorption and internalization of GO in J774A.1 cells. (A) Visualization of GO tracking at different time points. FITC-BSA-labeled GO post-treatment is visualized in green through confocal laser scanning microscopy. The cell membrane is stained in red with rhodamine-phalloidin, and cell nuclei are stained in blue with DAPI. Enlarged images in the right panel are representative of untreated cells and FITC-BSA-labeled S-GO-treated cells for 6 h. (B) Percentage of SSC values for GO-treated cells at 20 μg/mL over the time course relative to untreated cells. SSC values were determined by FACS analysis (n = 5).

S-GO failed to activate TLR4 signaling to induce TNF-α expression (Figure 9B). Taken together, these data demonstrated the crucial role of TLRs in sensing GO, and L-GO had a higher potential to activate TLR4 and subsequent pro-inflammatory effects than S-GO.

S-GO and L-GO Differentially Activated NF-κB Signaling. NF-κB signaling is mainly involved in TLR-activated gene expression that leads to macrophagic inflammation.[68] Upon TLR activation, IκB is phosphorylated and then subjected to ubiquitin-dependent proteasomal degradation, which promotes p65/RelA translocation from the cytoplasm into the nucleus, leading to enhanced transcription of targeted genes (Figure 9C).[69−71] In agreement with the above results, we found that GO could activate the NF-κB signaling pathway, as manifested by the reduction of IκB concentration in the cytosol and the increase of p65/RelA concentration in the nucleus compared to untreated cells (Figure 9D). Moreover, the L-GO showed stronger effects on the NF-κB pathway than S-GO (Figure 9D). To further clarify the contribution of NF-κB signaling to GO-conducted inflammation, a specific NF-κB inhibitor, pyrrolidine dithiocarbamate (PDTC, as illustrated in Figure 9C), was used to pretreat cells before GO exposure. As shown in Figure 9E, PDTC pretreatment significantly inhibited the induction of TNF-α expression by more than 50% for cells treated with S-GO or L-GO (P < 0.05). These data confirmed the crucial role of NF-κB signaling in the pro-inflammatory effects induced by GO. These data also reinforced the finding that L-GO, compared to S-GO, tends to adsorb plasma membrane with less cellular uptake, which enables greater activation of TLRs and NF-κB pathways to promote pro-inflammatory responses.

Additionally, reactive oxygen species (ROS) generation and oxidative stress have been shown to play an important role in stimulating the inflammatory responses (*e.g.*, enhanced secretion of inflammatory cytokines) through activation of NF-κB signaling.[72] Thus, ROS generation was also measured after GO treatment of macrophages. As shown in Supplementary Figure 10 and Figure 10A−C, both S-GO and L-GO could induce ROS production; however, there were no significant differences between them in acellular and cellular systems (P > 0.05). In addition to the effects on macrophages, the role of GO-induced oxidative stress in cytotoxicty was further verified in a variety of non-phagocytic cells, including mouse erythroleukemia (MEL) cells, human T-cell lymphoma (HUT102) cells, human Burkitt's lymphoma (RAMOS) cells and human liver carcinoma (HepG2) cells (Figure 10D). These results indicated that GO-induced ROS generation and oxidative stress are a general mechanism for cytotoxicity and pro-inflammatory effects for many cell types, which is important for GO hazard analysis *in vitro* and *in vivo*. It is worth noting that ROS greatly contribute to modulating various cellular processes including cell death and pro-inflammatory responses.[73,74] Although

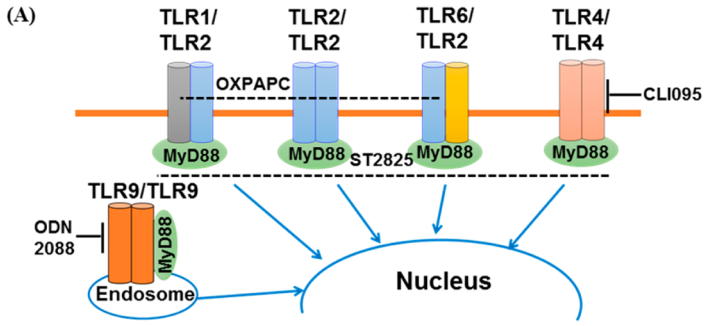

(B)

Inhibitors	Mechanism of action	TNF-α mRNA level
Inhibitor-free	-	1.00
OXPAPC	Block the signaling of TLR2 and TLR4	0.39 *
CLI095	Block the signaling mediated by the intracellular domain of TLR4	0.66 *
ODN2088	TLR9 Antagonist; Disrupt the co-localization of CpG ODNs with TLR9 in endosomal vesicles	1.04 NS
ST2825	Inhibit MyD88 dimerization and interfere with recruitment of IRAK1 and IRAK4 by MyD88, causing inhibition of IL-1beta-mediated activation of NF-κB transcriptional activity	0.30*

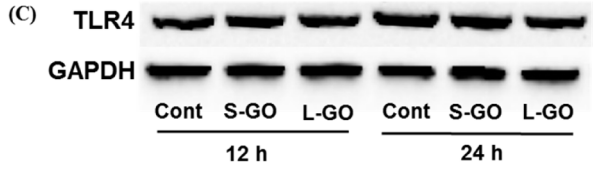

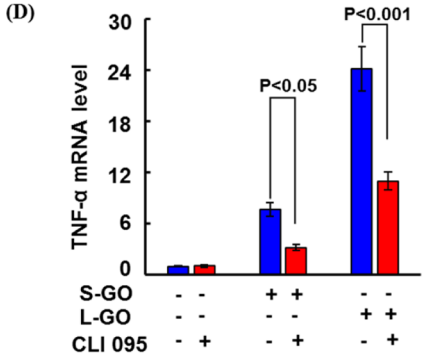

Figure 8. Membrane TLRs sense GO to trigger macrophagic inflammatory responses. (A) Schematic for the location of TLRs and the action sites of inhibitors. (B) TNF-α level in J774.A1 cells upon 20 μg/mL L-GO treatment for 24 h with or without pretreatment with different TLR inhibitors. (C) Western blot analysis of TLR4 concentration on the membrane after treatment with 20 μg/mL S-GO or L-GO for 12 and 24 h. (D) TNF-α level in J774.A1 cells upon S-GO or L-GO for 24 h with or without pretreatment with the TLR4 inhibitor (CLI095, 1 μg/mL). There were 6 replicates in each group ($n = 6$). Asterisk (*) means $P < 0.05$. ND: not detectable.

the detailed role of oxidative stress in GO-induced cytotoxicity and activation of inflammatory responses in macrophages is still not clear, our presented data suggest that the differential effects between S-GO and L-GO are likely due to the different localities or sites of ROS generation, devoid of significant difference in global ROS production.[75] For example, while S-GO is mostly taken up into the phagosomes to induce oxidative stress inside cells, L-GO on the cell surface may lead to membrane peroxidation in addition to oxidative stress inside cells. Further studies are thus warranted to clarify the role of ROS in these intertwined signaling pathways at different sites (such as on the membrane and inside cells) in response to different sized GO.

DISCUSSION

In this study, we compared the effects on M1 macrophage induction and pro-inflammation by GO with different lateral sizes *in vitro* and *in vivo*.

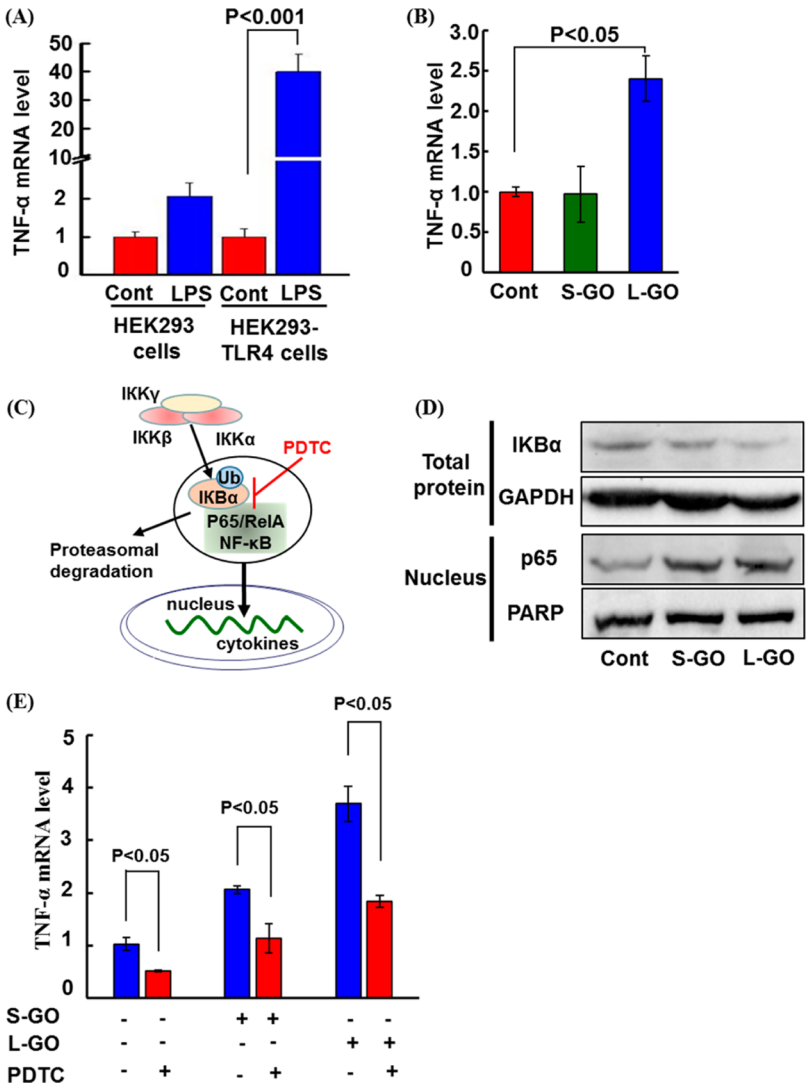

Figure 9. Differential activation of NF-κB signaling in response to GO size. (A) TNF-α expression in HEK293 cells and HEK293-TLR4 cells in response to LPS (1 μg/mL) for 12 h (n = 4). (B) TNF-α level in HEK293-TLR4 cells upon treatment with 40 μg/mL S-GO or L-GO for 24 h (n = 4). (C) Schematic diagram of NF-κB signaling and the action site of a NF-κB selective inhibitor, PDTC. (D) Western blotting results of IκBα concentration in total cellular proteins and p65 concentration in nuclear portion from J774.A1 cells treated with 20 μg/mL S-GO or L-GO for 24 h. (E) TNF-α level in J774.A1 cells treated with S-GO or L-GO at 20 μg/mL for 24 h with or without pretreatment with PDTC at 20 μM (n = 6).

We demonstrated that differently sized GO could cause differential pro-inflammatory effects *in vitro* and *in vivo*. We also determined the molecular mechanism underlying GO-induced inflammation. We found that, in comparison to its smaller counterpart, larger GO showed a stronger association with the plasma membrane, resulting in enhanced interaction with TLRs (*e.g.*, TLR4), which induces M1 polarization and triggers NF-κB activation to produce pro-inflammatory cytokines *in vitro* and inflammatory responses *in vivo* after GO administration into the abdominal cavity, lung, or bloodstream through the tail vein.

The major finding of this study is the delineation of the size-dependent M1 macrophage polarization and pro-inflammatory effects for GO and the detailed mechanisms of GO-induced macrophage activation. Although previous work on GO has shown that differently sized GO induced differential cytotoxicity and pro-fibrogenic effects *in vitro* and *in vivo*,[76] it is uncertain what physicochemical properties play a major role because these characteristics are often interconnected including surface oxidation states, surface reactivity, and lateral sizes. We circumvented this problem by preparing the GO samples with different lateral sizes from the same starting material. Comprehensive material characterizations proved that physicochemical properties of these GO sheets remained the same except for their lateral sizes. Using these well-prepared materials, we determined the detailed mechanisms behind the lateral-size-dependent pro-inflammatory effects of GO *in vitro* and *in vivo*. Although a few reports discussed the size-associated cellular responses of GO in macrophages,[10,11] the interaction between GO and the plasma membrane,

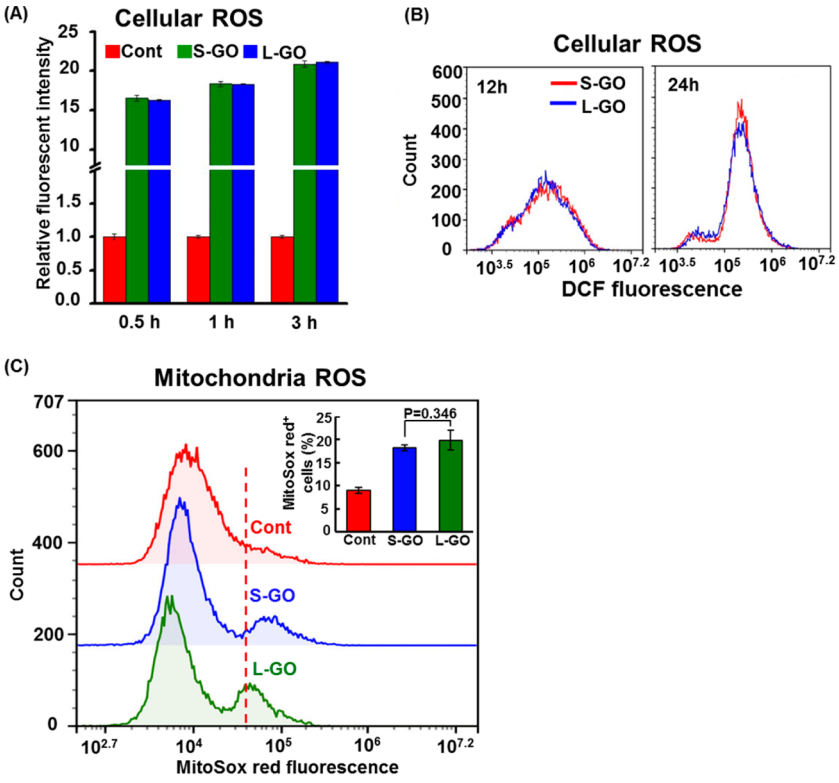

(D)

Cell type and derive	Cell line	Cell viability		ROS production	
		S-GO	L-GO	S-GO	L-GO
Mouse erythroleukemia	MEL	0.78±0.01	0.76±0.01	1.67±0.07	1.67±0.04
Human T-Cell lymphoma	HUT102	0.87±0.02	0.81±0.01	1.11±0.12	1.09±0.45
Human Burkitt's lymphoma	RAMOS	0.83±0.01	0.81±0.02	1.77±0.03	1.76±0.11
Human liver carcinoma	HepG2	0.79±0.05	0.78±0.03	1.23±0.10	1.24±0.12

Figure 10. Oxidative stress in response to different GO samples. (A) Intracellular ROS production in J774.A1 cells upon 20 μg/mL S-GO or L-GO at 0.5, 1, and 3 h. (B) FACS analysis of DCF fluorescence reflecting intracellular ROS generation in response to 20 μg/mL S-GO or L-GO for 12 and 24 h. (C) FACS analysis of MitoSox fluorescence in J774.A1 cells upon 20 μg/mL S-GO or L-GO for 24 h. Data were acquired from 20 000 cells per sample. Quantified data for MitoSox$^+$ cells were shown in the inset. There were 5 replicates in each group (n = 5). (D) Cell viability and ROS production upon GO. Cell viability of various types of nonphagocytic cells upon S-GO and L-GO at 20 μg/mL for 24 h through the live/dead viability/cytotoxicity assay (n = 6). ROS production was determined through FACS analysis of DCF fluorescence in cells upon 20 μg/mL S-GO or L-GO for 24 h (n = 5). Quantitative data show relative changes compared to untreated control.

cellular uptake, macrophage activation, and associated signaling transduction pathways remains unclear. We found that the mechanism involves lateral-size-dependent interaction between GO and TLRs on the plasma membrane and subsequent triggering of downstream NF-κB signaling pathways. While S-GO was more readily taken up by the cells, L-GO was inclined to associate with the cell membrane. This implies that the mechanism responsible for the differential cellular uptake behavior for both forms of GO could be different. There are reports indicating that particle shape and orientation play a key role in particle phagocytosis by macrophages.[77,78] For example, disk-shaped particles are readily phagocytosed by macrophages along their long axis when the particles first perpendicularly attach to the plasma membrane.[77,78] However, when their flat side has contact with the plasma membrane, the number of contact points with the membrane increases and particles will induce significant spreading of the cells without triggering phagocytosis.[77,78] Similarly, we postulate that this mechanism also applies for L-GO, which showed greater association with the plasma membrane on the flat side without being phagocytosed (Figure 6B). By contrast, for S-GO sheets, although they also have contact with the membrane by their flat side, the spreading of the cells is not substantial enough to inhibit the phagocytosis. As a result, the particles are still ingested without membrane association being shown (Figure 6B). Thus, we hypothesized that there is possibly a threshold for the GO lateral size that governs the occurrence of phagocytosis, namely, a counterbalance between

membrane spreading and cellular uptake; however, further detailed investigation is needed, and other parameters, such as bending rigidity and stiffness of the GO may also need to be taken into account. It is worth noting that GO, as a 2-D material with one-atom thickness, could also drive spontaneous membrane penetration at edges or corner sites.[79] Local piercing through these sharp protrusions decreases the energy barrier and facilitates the cellular uptake of GO.[79] To this end, S-GO could more readily pass through the membrane than L-GO, due to less energy needed.

Stimulation of TLRs (particularly TLR4) preferentially skews macrophage function toward the M1 phenotype predominantly through activation of the NF-κB pathway.[80] The M1 phenotype is characterized by feature alterations to macrophages, such as enhanced expression of pro-inflammatory cytokines, increased production of reactive nitrogen, and promotion of the Th1 response.[81] However, excessive or prolonged M1 polarization is harmful for the organism due to tissue injury and pathogenesis by overproduction of pro-inflammatory mediators.[82] Here, we demonstrated that larger GO could significantly activate TLRs (*e.g.*, TLR4) to promote macrophage M1 polarization through canonical NF-κB signaling, leading to enhanced pro-inflammatory responses. Although the detailed mechanism on how GO activates TLRs is still unclear, it may involve prolonged membrane association that allows multivalent interactions between the functionalized surface and TLRs on the cell membrane. Together, our data uncover an unrecognized toxicity mechanism for larger GO by promoting macrophage M1 polarization. These findings therefore suggest that the lateral size has to be taken into account for hazard assessment or biological/medical applications for GO and even other types of 2-D nanomaterials.

Another important finding of this work is that GO materials generated significant pro-inflammatory effects in mice *via* different exposure routes, including *ip*, *it*, and *iv* exposure. Lung was chosen because inhalation is the most common route for exposure to nanomaterials that become airborne, and the abdominal cavity has been used as a surrogate for the mesothelial lining of the chest cavity.[35] Meanwhile, *iv* exposure is a common route for administering medicine, and GO in fact is being developed for drug/gene delivery and bioimaging purposes.[3,4] Through all these exposure routes, we found that L-GO induced more potent inflammation to animals than S-GO. However, the mechanism responsible for the pro-inflammatory effects of these exposure routes may be different. For *ip* and *it* delivery, macrophages in peritoneal and lung play a major role, which involves induction of macrophage polarization into M1 subtype. For *iv* injection, this may involve monocytes/macrophages or other immune cells in distal tissues that have GO exposure; however, the detailed mechanism is still unknown, and further work is needed to clarify the mechanism. Despite the differences in delivery routes, we consistently showed that GO could induce inflammatory responses locally as well as systemically. In addition, our data suggest that it may be possible to modulate the inflammatory responses through controlling the lateral size to make GO safer, *e.g.*, by making GO even smaller while maintaining the desirable properties for use. This finding is important for considering future biological applications of GO.

CONCLUSIONS

We here demonstrated the lateral-size-dependent pro-inflammatory effects of GO *in vitro* and *in vivo*. The molecular mechanism of these effects involved a size-dependent interaction between GO and the plasma membrane. L-GO was prone to plasma membrane adsorption to activate the TLRs and NF-κB pathways, whereas S-GO was mostly taken up by macrophages. M1 polarization was a fundamental phenotype change to macrophages upon GO treatment, which enhances pro-inflammatory cytokine production and promotes recruitment of immune cells. We found that M1 induction by GO was dependent on its lateral size. Our study therefore indicates that fine-tuning of the lateral size of GO could be a safer design approach to increase its biocompatibility for biomedical applications.

METHODS AND EXPERIMENTAL SECTION

GO Preparation and Physiochemical Characterization. GO was produced from Asbury Mills 3061 grade graphite with a modified Hummer's method.[83] After oxidation, samples were washed, filtrated, and then centrifuged three times. Thereafter, dry GO powder was collected by freeze-drying. The concentration of GO solution was adjusted to 1 mg/mL with sterile water, followed by bath sonicator for 3 h with a 100 Hz, 200 W ultrasonic cleaner (KunShan, JiangSu, China) and with water changing every hour. To remove those not fully exfoliated into single-atom thick sheets, the samples were then centrifuged for 15 min at 2000*g* (multispeed centrifugation, Thermo, CL31R, Waltham, MA, USA), and the supernatant was collected. This procedure was repeated twice. The as-prepared GO samples were named larger-sized GO samples (L-GO). Afterward, L-GO was used as the substrate for the preparation of intermediate-sized GO (*i.e.*, I-GO) and smaller-sized GO (namely, S-GO). S-GO and I-GO were prepared through probe sonication (ultrasonic cell disrupter, Sciencet Z. JY G2-HNNingbo, China) with cycles of 15 s work and 15 s rest with an ultrasonic power of 65 W (50% amplitude) in ice for 2 min (I-GO) and 15 min (S-GO). For GO mass quantification, the gradient dilution method was used to prepare a standard curve using ultraviolet spectrophotometry (Shimadzu, UV-3600, Kyoto, Japan).

Morphology of the GO samples was visualized by atomic force microscopy (Bruker, MM3D Germany) and transmission electron microscopy (Hitachi, H7650, Japan). Surface charge of the samples, either suspended in Milli-Q water or in cell culture medium, was analyzed by a Zeta-sizer (Malvern Nano ZS, Malvern, UK). An ultraviolet−visible spectrophotometer

(Shimadzu) was used to measure the UV−vis absorption spectrum from 190 to 800 nm for GO samples at 10 μg/mL. The FTIR spectrum was applied to identify the presence of functional groups on the surface of GO samples. The spectrum was taken from 4000 to 400 cm^{-1} on an FTIR (Spectrum One, PerkinElmer Instruments Co. Ltd., USA). Additionally, GO samples were deposited onto silicon wafers, followed by air-drying, and then the air-dried silicon wafers were subjected to XPS. GO samples were also assessed by confocal micro-Raman spectroscopy, as previously reported.[84]

Preparation of FITC-BSA-Conjugated GO. GO was labeled with FITC-BSA following an established method.[85] Briefly, 1 mg of FITC-labeled BSA powder (five FITC per BSA) (Bioss Inc., Beijing, China) was dissolved in 1 mL of sterile water. GO samples and FITC-BSA solution were mixed with a mass ratio of 1:1 by gentle pipeting, followed by incubation at 37 °C with protection from light overnight. Thereafter, mixed solutions were centrifuged at 16000*g*, 4 °C, for 30 min. Afterward, the supernatant with free FITC-BSA was aspirated, and the pallets were then washed with cold PBS. This procedure was repeated three times. Finally, the collected pellets were resuspended in sterile water, and the concentration of FITC-BSA-conjugated GO was determined through an ultraviolet spectrophotometer.

Cell Culture. Mouse macrophage cell line J774A.1, human macrophage cell line THP-1, human embryo kidney cell line HEK293, mouse erythroleukemia (MEL) cells, human T-cell lymphoma (HUT102) cells, human Burkitt's lymphoma (RAMOS) cells, and human liver carcinoma (HepG2) cells were purchased from the Shanghai Cell Bank of Type Culture Collection of the Chinese Academy of Sciences. Cells were individually cultured in Dulbecco's modified Eagle's medium (DMEM) or RMPI 1640 (Hyclone), supplemented with 10% fetal bovine serum (FBS, Gibco) and 100 U/mL penicillin/streptomycin (Gibco). The HEK293/TLR4/MD2/CD14 (with the abbreviation HEK293-TLR4) cell line, originally derived from InvivoGen Inc. (San Diego, CA, USA), was generously provided by Dr. Shitao Li at Harvard Medical School.[66] HEK293-TLR4 cells were cultured in DMEM (Sigma-Aldrich) with 10% FBS, 100 units/mL of penicillin G, and 100 μg/mL of streptomycin.

FACS Analysis of Cell Populations. To clarify the nature of recruited cells in the abdominal cavity or lung, harvested cells were stained with antibodies (Abs): FITC-conjugated anti-mouse CD45, PerCP-conjugated anti-mouse CD54, APC-conjugated anti-mouse CD11b, PE-conjugated anti-mouse F4/80, or PE-conjugated anti-mouse Gr1. TruStain fcX (anti-mouse CD16/32) was used to block Fc receptors on cells. FITC-conjugated rat IgG2b, APC-conjugated rat IgG2b, PE-conjugated rat IgG2b, or PerCP-conjugated rat IgG2b were individually used as the isotype control in immunofluorescent staining. These Abs were purchased from BioLegend Inc. (San Diego, CA, USA). FACS analysis was performed on a BD FACSCalibur platform (BD Biosciences), according to standard protocols as previously described.[86]

Pretreatment of Inhibitors against TLRs or NF-κB Signaling. Regarding inhibition of TLR signaling, J774A.1 cells were pretreated for 6 h with the following inhibitors: OXPAPC (30 μg/mL; InvivoGen) to block the signaling of TLR2 and TLR4; CLI-095 (1 μg/mL; InvivoGen) to repress the signaling mediated by the intracellular domain of TLR4; ODN2088 (TLR9 antagonist) (10 μM; InvivoGen) to disrupt the colocalization of unmethylated CpG oligonucleotide (ODN) with TLR9 in endosomal vesicles; and ST2825 (5 μM; MedChemexpress Inc., Princeton, NJ, USA) to inhibit MyD88 dimerization and thus prevent the recruitment of IRAK1 and IRAK4 by MyD88. Cells were thereafter treated with 20 μg/mL GO for 24 h. In terms of inhibition of the NF-κB signaling, an NF-κB selective inhibitor, PDTC (Sigma), at a concentration of 20 μM was used to pretreat cells for 1.5 h prior to GO exposure.

Cell Viability Assay. To examine cell viability, cells were first seeded at a density of 0.8×10^4/well in 96-well plates (Corning Inc., NY, USA) at 37 °C overnight. Thereafter, cells were treated with GO. After 24 h incubation, cell viability was assayed with a live/dead viability/cytotoxicity kit following the instructions from the manufacturer (Invitrogen, Thermo Fisher Scientific Inc., USA).

Western Blotting. Post-treatment, cells were collected and washed with cold PBS. Cells were then lysed using the RIPA lysate buffer (Solarbio Inc., Beijing, China) containing protease inhibitor cocktail (Roche Inc., Switzerland). The concentrations of protein extracts were analyzed with the Lowery method (Solarbio). The same amount of proteins was subjected to 10% SDS-PAGE (Bio-Rad Inc., CA, USA) and then transferred onto nitrocellulose membranes. Western blot analysis was thus preformed, as described previously.[87] For the assay of the translocation of p65 into the nucleus, the nuclear proportion was separately collected with a nucleoprotein extraction kit (Solarbio). The Abs were anti-mouse p65 (1:1000, Bioss), anti-mouse IκBα (1:200, Bioss), anti-mouse TLR4 (1:200, Santa Cruz Biotechnology Inc.), anti-mouse GAPDH (1:1000, Zhong Shan Jin Qiao, Inc., China), and anti-mouse PARP (1:200, Bioss). GAPDH was used a loading control of total proteins, and poly(ADP-ribose) polymerase (PARP) was applied as a loading control for nuclear proteins.

qRT-PCR Analysis. Total RNAs were extracted from cells using Trizol according to the manufacturer's instruction (Invitrogen). The mRNA levels for genes including IL-6, IL-1β, and TNF-α were determined using SYBR Green qPCR mix (Promega Inc., USA) on an Mx3005P qRT-PCR instrument (Bio-Rad). Primers for PCR reactions are listed in Supplementary Table 1.

Intracellular Characterization of GO by Confocal Micro-Raman Spectroscopy. To characterize intracellular GO, confocal micro-Raman spectroscopy was performed. Cells were gently washed with PBS after GO treatment. After fixing with 2.5% glutaraldehyde, cells were excited with a 633 nm laser. Raman mapping was recorded on a 36×36 μm^2 area with a step size of 1 μm and acquisition time of 3 s under 10% power. The mapping images were obtained by collecting the Raman spectrum at each spot. The Raman mapping was also merged with its corresponding bright-field morphological image.

GO Tracking and Uptake Assessment through Confocal Laser Scanning Microscopy and FACS. To track GO localization and internalization, cells were exposed to FITC-BSA-labeled GO. After treatment for the indicted time, cells were washed with prewarmed PBS (at 37 °C) three times to remove GO stuck to the culture dish and loosely clinging to cells. Cells were then fixed with 3.7% paraformaldehyde in PBS for 10 min at room temperature, followed by incubation in PBS with 0.1% Triton X-100 and 1% BSA for 5 min. Cell nuclei were stained with DAPI (blue), and the plasma membrane was concomitantly stained with rhodamine-phalloidin (red). Fluorescent images were captured through confocal laser scanning microscopy on a TCS SP5 CLSM (Leica). Additionally, based on the established method for cellular uptake detection of carbon nanotubes,[56] cellular uptake of GO was determined through FACS analysis by assessing SSC values of cells upon treatment with non-FITC-labeled GO.

Macrophage Polarization Assessment through FACS. After treatment with 20 μg/mL S-GO or L-GO for 24 h, cells were collected and fixed with the cell fixative (Beyotime Inc., Beijing, China) for 15 min at room temperature. After washing with PBS three times, cells were permeabilized with 0.05% Triton 100 in PBS for 5 min and were then washed three times, followed by blocking with 0.5% BSA in PBS for 15 min at 4 °C. Cells were subsequently incubated with APC-conjugated anti-mouse Arg1 (Bioss) Ab or PE-conjugated anti-mouse iNOS (Bioss) Ab for 30 min and were washed three times prior to FACS analysis. APC-conjugated rat IgG2b or PE-conjugated rat IgG2b were accordingly used as the isotype control.

Animal Experiments. All animal care and experimental procedures were approved by the Animal Ethics Committee at the Research Center for Eco-Environmental Sciences, Chinese Academy of Sciences. BALB/c male mice (7 weeks old and with a body weight of about 20 g) were purchased from the Vital River Laboratory Animal Technology Co. Ltd., Beijing, China. To study inflammatory responses, mice were administrated with GO into the peritoneal cavity, lung, or bloodstream. For the *ip* administration of GO, GO was administrated at 5000 μg/kg body weight divided by two injections in 3 days. When mice were sacrificed, the abdominal cavities were washed with cold PBS according to a previous report.[35] The harvested lavages from the peritoneal cavities were subjected to RBC lysis with RBC lysate buffer (Solarbio), followed by cell number counting, FACS analysis, total protein assay, and inflammatory cytokine assessment by

ELISA. Blood was also collected for the determination of inflammatory cytokines in sera.

Lung exposure was carried out following the *it* method, as previously described.[56] In brief, anesthetized mice were instilled at the position of the back tongue with GO at a dose of 2500 μg/kg body weight. Mice were sacrificed 72 h post-GO administration, and bronchoalveolar lavage was harvested for cell number counting, total protein assay, FACS analysis, and inflammatory cytokine assessment, similar to the experiments with abdominal cavities. Regarding intratail vein injection, 5000 μg/kg body weight S-GO or L-GO was administrated. After 24 h treatment, mice were sacrificed and blood was collected for assessment of inflammatory cytokines in sera. The control group received saline only.

Cytokine Determination. The concentration of cytokines including IL-6, IL-1β, and TNF-α was determined in culture media, sera, lavages from peritoneal cavities, and BAL fluid with ELISA kits according to the manufacturer's instructions (R&D Systems).

ROS and MitoSox Assays. For ROS measurement, cells were cultured in 96-well plates and preincubated with 10 μM dichlorofluorescein-diacetate (DCF-DA, Sigma) for 30 min. Thereafter, cells were washed with PBS and subsequently treated with GO. At 0.5, 1, and 3 h post-GO treatment, DCF fluorescence was recorded at 525 nm using an excitation wavelength of 488 nm on a plate reader, as previously described.[8] Meanwhile, to assess the production of ROS for longer time, such as 12 and 24 h post-GO exposure, DCF probes were loaded into cells after GO treatment at the time points for detection, followed by FACS analysis as described.[8] MitoSox Red assay was carried to assess mitochondrial superoxide production of GO-treated cells following a standard protocol from the manufacturer (Molecular Probes, Invitrogen).

Statistical Analysis. An independent *t* test or one-way ANOVA test was applied to analyze the experimental data. Data are shown as the mean $\pm$ SE. Statistical significance was determined with a *P* value of less than 0.05.

Conflict of Interest: The authors declare no competing financial interest.

Acknowledgment. This work was supported by grants under the national "973" Program (Grant No. 2014CB932000) and the Strategic Priority Research Program of the Chinese Academy of Sciences (Grant No. XDB14000000) and grants from the National Natural Science Foundation of China (Grant Nos. 21425731, 21377159, 21177151, 21207152). T.X. is supported by the NIEHS RO1ES022698. We thank Drs. Jian Weng, Bingbing Sun, and Lingyun Zhao for critical reading of the manuscript. We thank all the laboratory members for their great assistance with experiments and reagents, and we thank Ms. Weilu Zhao for the preparation of the figures.

Supporting Information Available: The Supporting Information is available free of charge on the ACS Publications website at DOI: 10.1021/acsnano.5b04751.

Additional experimental results and primer sequences related to this work (PDF)

REFERENCES AND NOTES

1. Bitounis, D.; Ali-Boucetta, H.; Hong, B. H.; Min, D. H.; Kostarelos, K. Prospects and challenges of graphene in biomedical applications. *Adv. Mater.* **2013**, *25*, 2258–2268.
2. Bussy, C.; Ali-boucetta, H.; Kostarelos, K. Safety considerations for graphene: lessons learnt from carbon nanotubes. *Acc. Chem. Res.* **2013**, *46*, 692–701.
3. Gonçalves, G.; Vila, M.; Portolés, M. T.; Vallet-Regi, M.; Gracio, J.; Marques, P. A. A. P. Nano-Graphene Oxide: A Potential Multifunctional Platform for Cancer Therapy. *Adv. Healthcare Mater.* **2013**, *2*, 1072–1090.
4. Byun, J. Emerging Frontiers of Graphene in Biomedicine. *J. Microbiol. Biotechnol.* **2015**, *25*, 145–151.
5. Feng, L.; Liu, Z. Graphene in biomedicine: opportunities and challenges. *Nanomedicine (London, U. K.)* **2011**, *6*, 317–324.
6. Krishna, K. V.; Ménard-Moyon, C.; Verma, S.; Bianco, A. Graphene-based nanomaterials for nanobiotechnology and biomedical applications. *Nanomedicine (London, U. K.)* **2013**, *8*, 1669–1688.
7. Seabra, A. B.; Paula, A. J.; de Lima, R.; Alves, O. L.; Durán, N. Nanotoxicity of Graphene and Graphene Oxide. *Chem. Res. Toxicol.* **2014**, *27*, 159–168.
8. Qu, G. B.; Liu, S. J.; Zhang, S. P.; Wang, L.; Wang, X. Y.; Sun, B. B.; Yin, N. Y.; Gao, X.; Xia, T.; Chen, J. J.; et al. Graphene oxide induces toll-like receptor 4 (TLR4)-dependent necrosis in macrophages. *ACS Nano* **2013**, *7*, 5732–5745.
9. Bussy, C.; Ali-Boucetta, H.; Kostarelos, K. Safety Considerations for Graphene: Lessons Learnt from Carbon Nanotubes. *Acc. Chem. Res.* **2013**, *46*, 692–701.
10. Chang, Y. l.; Yang, S. T.; Liu, J. H.; Dong, E.; Wang, Y. W.; Cao, A.; Liu, Y. F.; Wang, H. F. In vitro toxicity evaluation of graphene oxide on A549 cells. *Toxicol. Lett.* **2011**, *200*, 201–210.
11. Yue, H.; Wei, W.; Yue, Z.; Wang, B.; Luo, N.; Gao, Y.; Ma, D.; Ma, G.; Su, Z. The role of the lateral dimension of graphene oxide in the regulation of cellular responses. *Biomaterials* **2012**, *33*, 4013–4021.
12. Kim, H.; Lee, D.; Kim, J.; Kim, T.; Kim, W. J. Photothermally triggered cytosolic drug delivery via endosome disruption using a functionalized reduced graphene oxide. *ACS Nano* **2013**, *7*, 6735–6746.
13. Maity, A. R.; Chakraborty, A.; Mondal, A.; Jana, N. R. Carbohydrate coated, folate functionalized colloidal graphene as a nanocarrier for both hydrophobic and hydrophilic drugs. *Nanoscale* **2014**, *6*, 2752–275 8.
14. Yang, L. J.; Wang, F.; Han, H.; Yang, L.; Zhang, G. S.; Fan, Z. Z. Functionalized graphene oxide as a drug carrier for loading pirfenidone in treatment of subarachnoid hemorrhage. *Colloids Surf., B* **2015**, *129*, 21–29.
15. Liu, Z.; Robinson, J. T.; Sun, X. M.; Dai, H. J. PEGylated nanographene oxide for delivery of water-insoluble cancer drugs. *J. Am. Chem. Soc.* **2008**, *130*, 10876–10877.
16. Becerril, H. A.; Mao, J.; Liu, Z. F.; Stoltenberg, R. M.; Bao, Z. N.; Chen, Y. S. Evaluation of Solution-Processed Reduced Graphene Oxide Films as Transparent Conductors. *ACS Nano* **2008**, *2*, 463–470.
17. Gurunathan, S.; Han, J. W.; Dayem, A. A.; Eppakayala, V.; Kim, J. H. Oxidative stress-mediated antibacterial activity of graphene oxide and reduced graphene oxide in Pseudomonas aeruginosa. *Int. J. Nanomed.* **2012**, 5901–5914.
18. Khanra, P.; Kuila, T.; Kim, N. H.; Bae, S. H.; Yu, D. S.; Lee, J. H. Simultaneous bio-functionalization and reduction of graphene oxide by baker's yeast. *Chem. Eng. J.* **2012**, *183*, 526–533.
19. Li, D.; Muller, M. B.; Gilje, S.; Kaner, R. B.; Wallace, G. C. Processable aqueous dispersions of graphene nanosheets. *Nat. Nanotechnol.* **2008**, *3*, 101–105.
20. Robinson, J. T.; Tabakman, S. M.; Liang, Y. Y.; Wang, H. L.; Sanchez Casalongue, H.; Vinh, D.; Dai, H. J. Ultrasmall Reduced Graphene Oxide with High Near-Infrared Absorbance for Photothermal Therapy. *J. Am. Chem. Soc.* **2011**, *133*, 6825–6831.
21. Luo, Z. T.; Lu, Y.; Somers, L. A.; Johnson, A. T. C. High Yield Preparation of Macroscopic Graphene Oxide Membranes. *J. Am. Chem. Soc.* **2009**, *131*, 898–899.
22. Jorio, A.; Cancado, L. G. Perspectives on Raman spectroscopy of graphene-based systems: from the perfect two-dimensional surface to charcoal. *Phys. Chem. Chem. Phys.* **2012**, *14*, 15246–15256.
23. Pimenta, M. A.; Dresselhaus, G.; Dresselhaus, M. S.; Cancado, L. G.; Jorio, A.; Saito, R. Studying disorder in graphite-based systems by Raman spectroscopy. *Phys. Chem. Chem. Phys.* **2007**, *9*, 1276–1291.
24. Perraki, M.; Proyer, A.; Mposkos, E.; Kaindl, R.; Hoinkes, G. Raman micro-spectroscopy on diamond, graphite and other carbon polymorphs from the ultrahigh-pressure metamorphic Kimi Complex of the Rhodope Metamorphic Province, NE Greece. *Earth Planet. Sci. Lett.* **2006**, *241*, 672–685.
25. Ferrari, A. C. Raman spectroscopy of graphene and graphite: Disorder, electron-phonon coupling, doping and

nonadiabatic effects. *Solid State Commun.* **2007**, *143*, 47–57.
26. Bokobza, L.; Bruneel, J. L.; Couzi, M. Raman spectroscopy as a tool for the analysis of carbon-based materials (highly oriented pyrolitic graphite, multilayer graphene and multiwall carbon nanotubes) and of some of their elastomeric composites. *Vib. Spectrosc.* **2014**, *74*, 57–63.
27. Sadezky, A.; Muckenhuber, H.; Grothe, H.; Niessner, R.; Pöschl, U. Raman microspectroscopy of soot and related carbonaceous materials: Spectral analysis and structural information. *Carbon* **2005**, *43*, 1731–1742.
28. Zhi, X.; Fang, H. L.; Bao, C. C.; Shen, G. X.; Zhang, J. L.; Wang, K.; Guo, S. W.; Wan, T.; Cui, D. X. The immunotoxicity of graphene oxides and the effect of PVP-coating. *Biomaterials* **2013**, *34*, 5254–5261.
29. Orecchioni, M.; Bedognetti, D.; Sgarrella, F.; Marincola, F.; Bianco, A.; Delogu, L. G. Impact of carbon nanotubes and graphene on immune cells. *J. Transl. Med.* **2014**, *12*, 138.
30. Yang, M.; Flavin, K.; Kopf, I.; Radics, G.; Hearnden, C. H. A.; McManus, G. J.; Moran, B.; Villalta-Cerdas, A.; Echegoyen, L. A.; Giordani, S.; et al. Functionalization of Carbon Nanoparticles Modulates Inflammatory Cell Recruitment and NLRP3 Inflammasome Activation. *Small* **2013**, *9*, 4194–4206.
31. Kool, M.; Soullie, T.; van Nimwegen, M.; Willart, M. A. M.; Muskens, F.; Jung, S.; Hoogsteden, H. C.; Hammad, H.; Lambrecht, B. N. Alum adjuvant boosts adaptive immunity by inducing uric acid and activating inflammatory dendritic cells. *J. Exp. Med.* **2008**, *205*, 869–882.
32. Yang, K.; Gong, H.; Shi, X. Z.; Wan, J. M.; Zhang, Y. J.; Liu, Z. In vivo biodistribution and toxicology of functionalized nano-graphene oxide in mice after oral and intraperitoneal administration. *Biomaterials* **2013**, *34*, 2787–2795.
33. Li, B.; Zhang, X. Y.; Yang, J. Z.; Zhang, Y. J.; Li, W. X.; Fan, C. H.; Huang, Q. Influence of polyethylene glycol coating on biodistribution and toxicity of nanoscale graphene oxide in mice after intravenous injection. *Int. J. Nanomed.* **2014**, *9*, 4697–4707.
34. Sydlik, S. A.; Jhunjhunwala, S.; Webber, M. J.; Anderson, D. G.; Langer, R. In Vivo Compatibility of Graphene Oxide with Differing Oxidation States. *ACS Nano* **2015**, *9*, 3866–3874.
35. Poland, C. A.; Duffin, R.; Kinloch, K.; Maynard, M.; Wallace, A. H. W.; Seaton, A.; Stone, V.; Brown, S.; MacNee, w.; Donaldson, K. Carbon nanotubes introduced into the abdominal cavity of mice show asbestoslike pathogenicity in a pilot study. *Nat. Nanotechnol.* **2008**, *3*, 423–428.
36. Ryman-Rasmussen, J. P.; Cesta, M. F.; Brody, A. R.; Shipley-Phillips, J. K.; Everitt, J. I.; Tewksbury, E. W.; Moss, O. R.; Wong, B. A.; Dodd, D. E.; Andersen, M. E.; et al. Inhaled carbon nanotubes reach the subpleural tissue in mice. *Nat. Nanotechnol.* **2009**, *4*, 747–751.
37. Gordon, S. Alternative activation of macrophages. *Nat. Rev. Immunol.* **2003**, *3*, 23–35.
38. Gautier, E. L.; Shay, T.; Miller, J.; Greter, M.; Jakubzick, C.; Ivanov, S.; Helft, J.; Chow, A.; Elpek, K. G.; Gordonov, S.; et al. Gene-expression profiles and transcriptional regulatory pathways that underlie the identity and diversity of mouse tissue macrophages. *Nat. Immunol.* **2012**, *13*, 1118–28.
39. Altin, J. G.; Sloan, E. K. The role of CD45 and CD45-associated molecules in T cell. *Immunol. Cell Biol.* **1997**, *75*, 430–445.
40. Gerhardt, T.; Ley, K. Monocyte trafficking across the vessel wall. *Cardiovasc. Res.* **2015**, *107*, 321–330.
41. Mocsai, A.; Walzog, B.; Lowell, C. A. Intracellular signaling during neutrophil recruitment. *Cardiovasc. Res.* **2015**, *107*, 373–385.
42. Vargas-Caraveo, A.; Perez-Ishiwara, D. G.; Martinez-Martinez, A. Chronic Psychological Distress as an Inducer of Microglial Activation and Leukocyte Recruitment into the Area Postrema. *NeuroImmunoModulation* **2015**, *22*, 311–321.
43. Schwarz, M.; Anela, T.; Nuru, E.; Shrikant, R. M.; Ramanjaneyulu, A.; Volker, V. Analysis of TNF-mediated recruitment and activation of glomerular dendritic cells in mouse kidneys by compartment-specific flow cytometry. *Kidney Int.* **2013**, *84*, 116–129.
44. Sandberg, W. J.; Låg, M.; Holme, J. A.; Friede, B.; Gualtieri, M.; Kruszewski, M.; Schwarze, P. E.; Skuland, T.; Refsnes, M. Comparison of non-crystalline silica nanoparticles in IL-1β release from macrophages. *Part. Fibre Toxicol.* **2012**, *9*, 32.
45. Moritz, E.; Norcia, Â. M. M. I.; Cardone, J. D. B.; Kuwano, S. T.; Chiba, A. K.; Yamamoto, M.; Bordin, J. O. Human neutrophil alloantigens systems. *An. Acad. Bras. Cienc.* **2009**, *81*, 559–569.
46. Zhang, L. L.; Fu, J. J.; Sheng, K. L.; Li, Y.; Song, S. S.; Li, P. P.; Song, S. S.; Wang, Q. T.; Chen, J. Y.; Yu, J. H.; et al. Bone marrow CD11b+F4/80+ dendritic cells ameliorate collagen-induced arthritis through modulating the balance between Treg and Th17. *Int. Immunopharmacol.* **2015**, *25*, 96–105.
47. Wynn, T. A.; Chawla, A.; Pollard, J. W. Macrophage biology in development, homeostasis and disease. *Nature* **2013**, *496*, 445–455.
48. Biswas, S. K.; Mantovani, A. Macrophage plasticity and interaction with lymphocyte subsets: cancer as a paradigm. *Nat. Immunol.* **2010**, *11*, 889–896.
49. Hoppstädter, J.; Seif, M.; Dembek, A.; Cavelius, C.; Huwer, H.; Kraegeloh, A. K. M2 polarization enhances silica nanoparticle uptake by macrophages. *Front. Pharmacol.* **2015**, *6*, 6.
50. Hayakawa, K.; Okazaki, R.; Morioka, K.; Nakamura, K.; Tanaka, S.; Ogata, T. Lipopolysaccharide preconditioning facilitates M2 activation of resident microglia after spinal cord injury. *J. Neurosci. Res.* **2014**, *92*, 1647–1658.
51. Penas, F.; Mirkin, G. A.; Vera, M.; Cevey, A.; Gonzalez, C. D.; Gomez, M. I.; Sales, M. E.; Goren, N. B. Treatment in vitro with PPARα and PPARγ ligands drives M1-to-M2 polarization of macrophages from T. cruzi-infected mice. *Biochim. Biophys. Acta, Mol. Basis Dis.* **2015**, *1852*, 893–904.
52. Gordon, S.; Taylor, P. R. Monocyte and macrophage heterogeneity. *Nat. Rev. Immunol.* **2005**, *5*, 953–64.
53. Ghassabeh, G. H.; Baetselier, P. D.; Brys, L.; Noël, W.; Ginderachter, J. A. V.; Meerschaut, S.; Beschin, A.; Brombacher, F.; Raes, G. Identification of a common gene signature for type II cytokine-associated myeloid cells elicited in vivo in different pathologic conditions. *Blood* **2006**, *108*, 575–583.
54. Cho, W. J.; Kim, Y.; Kim, J. K. Ultrahigh-Density Array of Silver Nanoclusters for SERS Substrate with High Sensitivity and Excellent Reproducibility. *ACS Nano* **2012**, *6*, 249–255.
55. Doudrick, K.; Nosaka, T.; Herckes, P.; Westerhoff, P. Quantification of graphene and graphene oxide in complex organic matrices. *Environ. Sci.: Nano* **2015**, *2*, 60–67.
56. Li, R. B.; Wang, X.; Ji, Z. X.; Sun, B. B.; Zhang, H. Y.; Chang, C. H.; Lin, S. J.; Meng, H.; Liao, Y. P.; Wang, M. Y.; et al. Surface Charge and Cellular Processing of Covalently Functionalized Multiwall Carbon Nanotubes Determine Pulmonary Toxicity. *ACS Nano* **2013**, *7*, 2352–2368.
57. Takeuchi, O.; Akira, S. Z. Pattern Recognition Receptors and Inflammation. *Cell* **2010**, *140*, 805–820.
58. Kawai, T.; Akira, S. Z. The roles of TLRs, RLRs and NLRs in pathogen recognition. *Int. Immunol.* **2009**, *21*, 317–337.
59. Kawai, T.; Akira, S. Z. Pathogen recognition with Toll-like receptors. *Curr. Opin. Immunol.* **2005**, *17*, 338–344.
60. Pasare, C.; Medzhitov, R. Toll-like receptors: linking innate and adaptive immunity. *Microbes Infect.* **2004**, *6*, 1382–1387.
61. Kang, J. Y.; Nan, X. H.; Jin, M. S.; Youn, S. J.; Ryu, Y. H.; Mah, S.; Han, S. H.; Lee, H. S.; Paik, S. G.; Lee, J. O. Recognition of Lipopeptide Patterns by Toll-like Receptor 2-Toll-like Receptor 6 Heterodimer. *Immunity* **2009**, *31*, 873–884.
62. Park, B. S.; Song, D. H.; Kim, H. M.; Choi, B. S.; Lee, H.; Lee, J. O. The structural basis of lipopolysaccharide recognition by the TLR4–MD-2 complex. *Nature* **2009**, *458*, 1191–1195.
63. Brodsky, I.; Medzhitov, R. Two Modes of Ligand Recognition by TLRs. *Cell* **2007**, *130*, 979–981.
64. Loiarro, M.; Capolunghi, F.; Fanto, N.; Gallo, G.; Campo, S.; Arseni, B.; Carsetti, R.; Carminati, P.; De Santis, R.; Ruggiero, V.; et al. Inhibition of MyD88 dimerization and recruitment of IRAK1 and IRAK4 by a novel peptidomimetic compound. *J. Leukocyte Biol.* **2007**, *82*, 801–10.

65. Chen, G. Y.; Yang, H. J.; Lu, C. H.; Chao, Y. C.; Hwang, S. M.; Chen, C. L.; Lo, K. W.; Sung, L. Y.; Luo, W. Y.; Tuan, H. Y.; et al. Simultaneous induction of autophagy and toll-like receptor signaling pathways by graphene oxide. *Biomaterials* **2012**, *33*, 6559–6569.
66. Li, S. T.; Wang, L. Y.; Berman, M.; Kong, Y. Y.; Dorf, M. E. Mapping a Dynamic Innate Immunity Protein Interaction Network Regulating Type I Interferon Production. *Immunity* **2011**, *35*, 426–440.
67. Guha, M.; Mackman, N. LPS induction of gene expression in human monocytes. *Cell. Signalling* **2001**, *13*, 85–94.
68. Mano, S. S.; Kanehira, K.; Taniguchi, A. Comparison of Cellular Uptake and Inflammatory Response via Toll-Like Receptor 4 to Lipopolysaccharide and Titanium Dioxide Nanoparticles. *Int. J. Mol. Sci.* **2013**, *14*, 13154–13170.
69. Zhang, J. M.; Zhu, J. P.; Imrich, A.; Cushion, M.; Kinane, T. B.; Koziel, H. Pneumocystis activates human alveolar macrophage NF-kappaB signaling through mannose receptors. *Infect. Immun.* **2004**, *72*, 3147–3160.
70. Nair, K. L.; Thulasidasan, A. K. T.; Deepa, G.; Anto, R. J.; Kumar, G. S. V. Purely aqueous PLGA nanoparticulate formulations of curcumin exhibit enhanced anticancer activity with dependence on the combination of the carrier. *Int. J. Pharm.* **2012**, *425*, 44–52.
71. Chen, G. Y.; Chen, C. L.; Tuan, H. Y.; Yuan, P. X.; Li, K. C.; Yang, H. J.; Hu, Y. C. Graphene oxide triggers toll-like receptors/autophagy responses in vitro and inhibits tumor growth in vivo. *Adv. Healthcare Mater.* **2014**, *3*, 1486–1495.
72. Buelna-Chontal, M.; Zazueta, C. Redox activation of Nrf2 & NF-kappaB: a double end sword? *Cell. Signalling* **2013**, *25*, 2548–2557.
73. Zhou, R. B.; Yazdi, A. S.; Menu, P.; Tschopp, J. A role for mitochondria in NLRP3 inflammasome activation. *Nature* **2011**, *469*, 221–225.
74. Sorbara, M. T.; Girardin, S. E. Mitochondrial ROS fuel the inflammasome. *Cell Res.* **2011**, *21*, 558–560.
75. Terada, L. S. Specificity in reactive oxidant signaling: think globally, act locally. *J. Cell Biol.* **2006**, *174*, 615–623.
76. Wang, X.; Duch, M. C.; Mansukhani, N.; Ji, Z. X.; Liao, Y. P.; Wang, M. Y.; Zhang, H. Y.; Sun, B. B.; Chang, C. H.; Li, R. B.; et al. Use of a Pro-Fibrogenic Mechanism-Based Predictive Toxicological Approach for Tiered Testing and Decision Analysis of Carbonaceous Nanomaterials. *ACS Nano* **2015**, *9*, 3032–3043.
77. Champion, J. A.; Mitragotri, S. Role of target geometry in phagocytosis. *Proc. Natl. Acad. Sci. U. S. A.* **2006**, *103*, 4930–4934.
78. Doshi, N.; Samir, M. Macrophages Recognize Size and Shape of Their Targets. *PLoS One* **2010**, *5*, e10051.
79. Li, Y. F.; Yuan, H. Y.; Bussche, A. V. D.; Creighton, M.; Hurt, R. H.; Kane, A. B.; Gao, H. J. Graphene microsheets enter cells through spontaneous membrane penetration at edge asperities and corner sites. *Proc. Natl. Acad. Sci. U. S. A.* **2013**, *110*, 12295–12300.
80. Wang, N.; Liang, H.; Zen, K. Molecular mechanisms that influence the macrophage m1-m2 polarization balance. *Front. Immunol.* **2014**, *5*, 614.
81. Sica, A.; Mantovani, A. Macrophage plasticity and polarization: in vivo veritas. *J. Clin. Invest.* **2012**, *122*, 787–795.
82. Murray, P. J.; Wynn, T. A. Protective and pathogenic functions of macrophage subsets. *Nat. Rev. Immunol.* **2011**, *11*, 723–737.
83. Chopra, P.; Bajpai, M.; Dastidar, S. G.; Ray, A. Development of a cell death-based method for the screening of nuclear factor-κB inhibitors. *J. Immunol. Methods* **2008**, *335*, 126–131.
84. Liu, R.; Liu, J. F.; Zhou, X. X.; Sun, M. T.; Jiang, G. B. Fabrication of a Au Nanoporous Film by Self-Organization of Networked Ultrathin Nanowires and Its Application as a Surface-Enhanced Raman Scattering Substrate for Single-Molecule Detection. *Anal. Chem.* **2011**, *83*, 9131–9137.
85. Mu, Q. X.; Su, G. X.; Li, L. W.; Gilbertson, B. O.; Yu, L. H.; Zhang, Q.; Sun, Y. P.; Yan, B. Size-dependent cell uptake of protein-coated graphene oxide nanosheets. *ACS Appl. Mater. Interfaces* **2012**, *4*, 2259–2266.
86. Wang, X. Y.; Wang, L. X.; Liu, S. J. Heme-Regulated eIF2α Kinase Plays a Crucial Role in Protecting Erythroid Cells against Pb-Induced Hemolytic Stress. *Chem. Res. Toxicol.* **2015**, *28*, 460–469.
87. Liu, S. J.; Goldstein, R. H.; Scepansky, E. M.; Rosenblatt, M. Inhibition of rho-associated kinase signaling prevents breast cancer metastasis to human bone. *Cancer Res.* **2009**, *69*, 8742–8751.